Consistent treatment of viscoelastic effects at junctions in one-dimensional blood flow models

Lucas O. Müller[a,b,*], Günter Leugering[c], Pablo J. Blanco[a,b]

[a] *Computer Science Department, National Laboratory for Scientific Computing, LNCC/MCTI, Av. Getúlio Vargas 333, 25651-075, Petrópolis, RJ, Brazil.*
[b] *INCT-MACC, Institute of Science and Technology in Medicine Assisted by Scientific Computing, Petrópolis, Brazil.*
[c] *Institute of Applied Mathematics 2, Friedrich-Alexander University of Erlangen-Nürnberg (FAU), Erlangen, Germany.*

Abstract

While the numerical discretization of one-dimensional blood flow models for vessels with viscoelastic wall properties is widely established, there is still no clear approach on how to couple one-dimensional segments that compose a network of viscoelastic vessels. In particular for Voigt-type viscoelastic models, assumptions with regard to boundary conditions have to be made, which normally result in neglecting the viscoelastic effect at the edge of vessels. Here we propose a coupling strategy that takes advantage of a hyperbolic reformulation of the original model and the inherent information of the resulting system. We show that applying proper coupling conditions is fundamental for preserving the physical coherence and numerical accuracy of the solution in both academic and physiologically relevant cases.

Keywords: Finite volume schemes, viscoelasticity, junctions, one-dimensional blood flow.

1. Introduction

The viscoelastic behavior of arterial and venous walls is well-known [1, 2, 3]. It has an impact on fundamental hemodynamic characteristics of the cardiovascular system [4] and plays a determinant role in setting the functional level of the cardiovascular system under physiological and, especially, under pathological conditions such as hypertension [5].

Among the many theoretical frameworks developed by applied mathematicians and biomedical engineers to study the cardiovascular system, one-dimensional blood flow models constitute a relevant tool which has been utilized since the late 70s to gain understanding on arterial functioning [6, 7, 8, 9]. More recent contributions to the development of one-dimensional models for the arterial and venous systems can be found in [10, 11, 12, 13, 14, 15, 16]. These models have been used to study a number of pathologies, some examples can be found in [17, 18, 19, 20, 21, 22, 23, 24]. Moreover, the output of such models has been validated versus *in vitro* models [25] and *in vivo* measurements [10, 14].

It is well known that blood flow in large to medium vessels is a convection-dominated process. Therefore most practitioners neglect viscoelasticity of vessel walls in their one-dimensional models. The resulting model is then essentially a hyperbolic system of partial differential equations and its numerical approximation is ruled by well-established strategies on this field. However, when certain models of vessel wall viscoelasticity are used [12, 16, 25, 26, 27], a second order

* Corresponding author
Email address: lmuller@lncc.br (Lucas O. Müller)

spatial derivative of the flow in the momentum balance equation arises, turning the problem into a convection-diffusion-reaction problem. The way by which the diffusive term is treated varies considerably from work to work. However, in all cases there is an assumption for the treatment of the diffusive term in correspondence of terminal edges, that is at those points of networks usually called junctions. In previous works, viscoelasticity was neglected in the coupling conditions applied in correspondence of junctions [12, 13, 25, 26, 28]. Such assumptions can be reasonable in certain situations, but, as shown in this work, they can be extremely harmful with regard to the physical consistency of the approximate solution.

Here we propose a coupling strategy based on the hyperbolic reformulation of a Voigt-type model for one-dimensional blood flow in viscoelastic vessels [31]. The proposed approach makes use of information that can be extracted from the eigenstructure of the resulting hyperbolic system. Moreover, junctions/bifurcations of vessels are considered as Riemann problems for which an exact/approximate solver can be devised. This kind of coupling strategy was proposed in [32] for one-dimensional blood flow in elastic vessels and is extended here to the viscoelastic case. Moreover, we propose an improved version of the data extrapolation step in which the interaction between vessels sharing a vertex is taken into account for both the leading term and the spatial derivatives of the Taylor series expansion. The numerical accuracy of the proposed methodology is verified by empirical convergence tests, as well as by a suite of tests on simple vessel networks. In addition, we apply the proposed methodology to an *in vitro* arterial network model [25, 33] and to an anatomically detailed model of the vasculature of the upper limb [34]. Computational results are compared to the solution delivered by applying a commonly used approach, the operator splitting technique, in order to assess the influence of neglecting the contribution of viscoelasticity at vessels edges on the several proposed tests. The principal goal of the presented tests is to show that the physical consistency of the model can be lost when the viscoelastic effect at junctions is not properly addressed.

The rest of the paper is structured as follows. The one-dimensional blood flow model, as well as its hyperbolic reformulation, is presented in Section 2. Next, the numerical methodology used to solve the underlying model within one-dimensional domains and the coupling strategy are described in Section 3. In Section 4 a series of tests is performed in order to assess the consistency and accuracy of the proposed methodology in the context of academic and physiological tests.

2. Mathematical model

In this section we present a well-known one-dimensional blood flow model featuring viscoelastic behavior of the vessel wall, as well as its hyperbolic reformulation. We then provide a brief description of the eigenstructure of the resulting PDE system, since the proposed coupling strategy between one-dimensional domains will be based on the inherent properties of the hyperbolized model.

2.1. 1D viscoelastic model

One-dimensional blood flow is modeled as

$$\begin{cases} \partial_t A + \partial_x q = 0\,, \\ \partial_t q + \partial_x \left(\dfrac{q^2}{A} \right) + \dfrac{A}{\rho} \partial_x p = -\dfrac{f}{\rho}\,, \end{cases} \tag{1}$$

where x is the axial coordinate along the longitudinal axis of the vessel; t is time; $A(x,t)$ is the cross-sectional area of the vessel; $q(x,t)$ is the flow rate; $p(x,t)$ is the average fluid pressure over

a cross-section; $f(x,t) = \gamma\pi\mu\frac{q}{A}$ is the friction force per unit length of the tube, with γ depending on the velocity profile; μ is the fluid viscosity and ρ is the fluid density.

To close the system of equations we adopt a tube law relating p to A and other parameters, namely

$$p(x,t) = p_r(x,t) + \zeta(x,t). \tag{2}$$

Here, $p_r(x,t) = p_0 + \delta p_{ext}(x,t)$ accounts for a homeostatic equilibrium pressure p_0, for which quantities with subscript "0" are defined, and fluctuations due to external tissues $\delta p_{ext}(x,t)$. In turn, $\zeta(x,t)$ accounts for the constitutive law of the vessel tissue, namely

$$\zeta(x,t) = \frac{\pi R_0 h_0}{A_d}\left[E_e\varepsilon + E_c\epsilon_r \ln(e^{\chi}+1) + \frac{K_m}{2\sqrt{AA_0}}\frac{\partial A}{\partial t}\right], \tag{3}$$

where $R_0 = R_0(x)$ is the vessel radius at reference state, obviously related to the reference cross-section area $A_0 = A_0(x)$ and $h_0 = h_0(x)$ is the vessel wall thickness at reference state. $E_e = E_e(x)$ is the effective Young modulus of the elastin, $E_c = E_c(x)$ is the effective Young modulus of the collagen and K_m is the effective viscoelastic parameter. In expression (3) $\chi = \chi(A;x)$ is

$$\chi = \frac{\varepsilon - \varepsilon_0}{\epsilon_r}, \tag{4}$$

where $\varepsilon_0 = \varepsilon_0(A_0)$ is the deformation state for which 50% of collagen fibers have been activated, $\epsilon_r = \epsilon_r(A_0)$ is the standard deviation of the fiber activation state distribution and $\varepsilon = \varepsilon(A;A_0)$ is the current deformation state, given by

$$\varepsilon = \sqrt{\frac{A}{A_0}} - 1. \tag{5}$$

Note that setting $A_d = 3/4\,A_0$ and $E_c = 0$ one obtains a widely used constitutive law, which shows a linear dependence of the elastic component of pressure with respect to the vessel radius. See for example [11, 25, 35, 36] . On the other hand, taking $A_d = A$ and $E_c \neq 0$, results in a tube law that considers the incompressibility of the vessel wall and thus the reduction of wall thickness as the vessel wall is stretched. As well, it provides a rational approach towards modeling the vessel wall by considering its structural components (elastin, collagen and smooth muscle cells). See for example [12, 13, 34].

2.2. Hyperbolic reformulation

By using the mass conservation equation in (1), one can replace the time derivative of A in (3) by the spatial derivative of the flow q. Replacing (2) in the momentum equation in (1) results in a set of PDEs containing second order derivatives. The way this term is treated at vessels edges, especially at junctions, is not clearly established in the literature, as previously discussed in Section 1.

Note that coupling conditions in the case $K_m = 0$, *i.e.* for purely elastic vessels, can be easily determined by the hyperbolic nature of the system, and the task of assigning coupling conditions at a point shared by several one-dimensional domains can be seen as a Riemann problem, as proposed in [32, 37]. Motivated by these works, here we adopt hyperbolic reformulation of (1)-(5) proposed in [31]. In order to obtain a first order PDE system we introduce the auxiliary variable θ, a relaxation time $T > 0$ and an evolution equation

$$\partial_t\theta = \frac{1}{T}(\partial_x q - \theta), \tag{6}$$

such that

$$\theta \to \partial_x q\,, \qquad T \to 0\,. \tag{7}$$

As reported in [31], in order to ensure that the formulation error is smaller than the discretization error the following relation must hold

$$\triangle := \frac{T}{(\Delta x)^p}\frac{1-2^{-\frac{1}{2}}}{2^{p-\frac{1}{2}}-1} = O(1)\,, \tag{8}$$

where p is the order of accuracy of the numerical scheme.

Now, ζ is

$$\zeta(x,t) = \frac{\pi R_0 h_0}{A_d}\left[E_e\varepsilon + E_c\epsilon_r \ln(e^{\chi}+1) - \frac{K_m}{2\sqrt{AA_0}}\theta\right] \tag{9}$$

and we can write (1) together with (2)-(5) as

$$\partial_t \mathbf{Q} + \mathbf{A}(\mathbf{Q})\partial_x \mathbf{Q} = \mathbf{S}(\mathbf{Q})\,, \tag{10}$$

where the augmented state vector is

$$\mathbf{Q} = \left[A, q, \theta, A_0, h_0, E_e, E_c, p_r\right]^T. \tag{11}$$

Note that we have introduced mechanical and geometrical parameters of the tube law as components of the augmented state vector $\mathbf{Q}$. This implies that we consider the trivial evolution equations $\partial_t \alpha = 0$, with $\alpha = A_0, h_0, E_e, E_c$ and $\partial_t p_r = F(x,t)$, with $F(x,t)$ prescribed. By doing so one incorporates the variation of vessel mechanical and geometrical properties into the eigenstructure of the system. Such approach allows the development of numerical schemes that correctly deal with discontinuous variations in these parameters. This approach was propose by [38] for a similar tube law and is applied here to system (1) with tube law given by (9). The coefficient matrix $\mathbf{A}(\mathbf{Q})$ of (10) is

$$\mathbf{A}(\mathbf{Q}) = \begin{bmatrix} 0 & 1 & 0 & 0 & 0 & 0 & 0 & 0 \\ c^2-u^2 & 2u & \frac{A}{\rho}\zeta_\theta & \frac{A}{\rho}\zeta_{A_0} & \frac{A}{\rho}\zeta_{h_0} & \frac{A}{\rho}\zeta_{E_e} & \frac{A}{\rho}\zeta_{E_c} & \frac{A}{\rho} \\ 0 & -\frac{1}{T} & 0 & 0 & 0 & 0 & 0 & 0 \\ 0 & 0 & 0 & 0 & 0 & 0 & 0 & 0 \\ 0 & 0 & 0 & 0 & 0 & 0 & 0 & 0 \\ 0 & 0 & 0 & 0 & 0 & 0 & 0 & 0 \\ 0 & 0 & 0 & 0 & 0 & 0 & 0 & 0 \\ 0 & 0 & 0 & 0 & 0 & 0 & 0 & 0 \end{bmatrix}, \tag{12}$$

with $c = \sqrt{\frac{A}{\rho}\zeta_A}$, $u = \frac{q}{A}$ and $\zeta_\alpha = \partial_\alpha \zeta$, with $\alpha = A, \theta, A_0, h_0, E_e, E_c$.

The source vector $\mathbf{S}(\mathbf{Q})$ is

$$\mathbf{S}(\mathbf{Q}) = [0, f, -\frac{\theta}{T}, 0, 0, 0, 0, F]^T. \tag{13}$$

Standard eigenstructure analysis shows that system (10) with coefficient matrix (12) is hyperbolic if

$$\zeta_A - \frac{\zeta_\theta}{T} > 0\,, \tag{14}$$

with eigenvalues

$$\lambda_1 = u - c_T\,, \quad \lambda_2 = \lambda_3 = \lambda_4 = \lambda_5 = \lambda_6 = \lambda_7 = 0\,, \quad \lambda_8 = u + c_T\,, \tag{15}$$

where

$$c_T = \sqrt{c^2 - \frac{A\zeta_\theta}{\rho T}}, \tag{16}$$

and linearly independent eigenvectors

$$\begin{aligned}
\mathbf{R}_1 &= \gamma_1 \begin{bmatrix} 1 \\ u - c_T \\ -\frac{1}{T} \\ 0 \\ 0 \\ 0 \\ 0 \\ 0 \end{bmatrix}, \quad \mathbf{R}_2 = \gamma_2 \begin{bmatrix} 0 \\ 0 \\ 0 \\ 1 \\ 0 \\ 0 \\ 0 \\ -\zeta_{A_0} \end{bmatrix}, \quad \mathbf{R}_3 = \gamma_3 \begin{bmatrix} 0 \\ 0 \\ 0 \\ 0 \\ 1 \\ 0 \\ 0 \\ -\zeta_{h_0} \end{bmatrix}, \quad \mathbf{R}_4 = \gamma_4 \begin{bmatrix} 0 \\ 0 \\ 0 \\ 0 \\ 0 \\ 1 \\ 0 \\ -\zeta_{E_e} \end{bmatrix}, \\
\mathbf{R}_5 &= \gamma_5 \begin{bmatrix} 0 \\ 0 \\ 0 \\ 0 \\ 0 \\ 0 \\ 1 \\ -\zeta_{E_c} \end{bmatrix}, \quad \mathbf{R}_6 = \gamma_6 \begin{bmatrix} 1 \\ 0 \\ 0 \\ 0 \\ 0 \\ 0 \\ 0 \\ \frac{\rho(u^2 - c^2)}{A} \end{bmatrix}, \quad \mathbf{R}_7 = \gamma_7 \begin{bmatrix} 0 \\ 0 \\ 1 \\ 0 \\ 0 \\ 0 \\ 0 \\ -\zeta_\theta \end{bmatrix}, \quad \mathbf{R}_8 = \gamma_8 \begin{bmatrix} 1 \\ u + c_T \\ -\frac{1}{T} \\ 0 \\ 0 \\ 0 \\ 0 \\ 0 \end{bmatrix},
\end{aligned} \tag{17}$$

where γ_i, for $i = 1, \ldots, 8$, are arbitrary scaling factors.

In what follows we will study the nature of characteristic fields of system (10), which are essential for defining wave relations, needed for the construction of numerical fluxes or Riemann problem solvers in general. A characteristic field associated to λ_k is said to be genuinely non-linear if

$$\nabla_{\mathbf{Q}} \lambda_k \cdot \mathbf{R}_k \neq 0, \tag{18}$$

for all $\mathbf{Q}$. For $k = 1$, the scalar product of the gradient of eigenvalue λ_1 with respect to $\mathbf{Q}$ and $\mathbf{R}_1$ is

$$-\frac{\partial c_T}{\partial A} - \frac{c_T}{A} + \frac{1}{T}\frac{\partial c_T}{\partial \theta} \neq 0, \tag{19}$$

for which a closed-form proof for the entire state and parameter spaces could not be obtained. However, this property was empirically observed for parameters and state variables in physiological ranges. Analogous consideration are valid for the characteristic field associated to λ_8. Finally, it is straightforward to show that characteristic fields associated to λ_2 to λ_7 are linearly degenerate since $\lambda_k = 0$ for $k = 2, 3, \ldots, 7$.

Generalized Riemann invariants associated to the k-th characteristic field are functions $\Gamma_k(\mathbf{Q})$ that satisfy the PDE

$$\nabla_{\mathbf{Q}} \Gamma_k(\mathbf{Q}) \cdot \mathbf{R}_k \equiv 0. \tag{20}$$

For the definition of generalized Riemann invariants for genuinely non-linear fields we follow the approach described in [39]. An integral curve of the vector field $\mathbf{R}_k$, associated to the eigenvalue λ_k, is defined as a smooth curve $\tilde{\mathbf{Q}}(\xi)$ in state space parametrized by a scalar parameter ξ, if at each point $\tilde{\mathbf{Q}}(\xi)$, the tangent vector to the curve is a parametrization of $\mathbf{R}_k$ [39], *i.e.*

$$\frac{d\tilde{\mathbf{Q}}(\xi)}{d\xi} = \alpha(\xi)\mathbf{R}_k, \tag{21}$$

where $\alpha(\xi)$ is a scaling factor.

If one sets $\alpha \equiv 1$ and considers the characteristic field associated to λ_1, then (21) is

$$\frac{d\tilde{A}(\xi)}{d\xi} = 1, \tag{22}$$

$$\frac{d\tilde{q}(\xi)}{d\xi} = \frac{q}{A} - c_T, \tag{23}$$

$$\frac{d\tilde{\theta}(\xi)}{d\xi} = -\frac{1}{T}, \tag{24}$$

$$\frac{d\tilde{A}_0(\xi)}{d\xi} = \frac{d\tilde{h}_0(\xi)}{d\xi} = \frac{d\tilde{E}_e(\xi)}{d\xi} = \frac{d\tilde{E}_c(\xi)}{d\xi} = \frac{d\tilde{p}_r(\xi)}{d\xi} = 0. \tag{25}$$

From the solution of (25) for A_0, h_0,E_e, E_c and p_r the invariance of those variables across nonlinear waves follows. Next we set

$$\tilde{A}(\xi) = \xi \tag{26}$$

in order to satisfy (22). By doing so we have chosen to parametrize the curve by area A. It follows immediately that

$$\tilde{\theta}(\xi) = -\frac{\xi}{T} + constant. \tag{27}$$

If we now fix a point in state space $\hat{\mathbf{Q}} = [\hat{A}, \hat{A}\hat{u}, \hat{\theta}, \hat{A}_0, \hat{h}_0, \hat{E}_e, \hat{E}_c, \hat{p}_r]^T$, then one can write the particular solution to (24), namely

$$\tilde{\theta}(\xi) = \hat{\theta} + \frac{\hat{A}}{T} - \frac{\xi}{T}. \tag{28}$$

Considering (26) and (28), the solution to (23) can be written as

$$\tilde{q}(\xi) = \xi\tilde{u}(\xi) = \xi\hat{u} - \xi\int_{\hat{A}}^{\tilde{A}(\xi)} \frac{\tilde{c}_T(\xi)}{\xi} d\xi, \tag{29}$$

with

$$\tilde{c}_T(\xi) = c_T(\xi, \tilde{\theta}(\xi)). \tag{30}$$

After some manipulations we have

$$\tilde{u}(\xi) = \hat{u} + \int_{\tilde{A}(\xi)}^{\hat{A}} \frac{\tilde{c}_T(\xi)}{\xi} d\xi. \tag{31}$$

Summarizing, we can state that generalized Riemann invariants for characteristic field associated to λ_1 are

$$\begin{aligned} &\Gamma_1^1 = u + \int_{\hat{A}}^{A} \frac{\tilde{c}_T(\xi)}{\xi} d\xi, \quad \Gamma_1^2 = \theta + \frac{A}{T}, \\ &\Gamma_1^3 = A_0, \quad \Gamma_1^4 = h_0, \quad \Gamma_1^5 = E_e, \\ &\Gamma_1^6 = E_c, \quad \Gamma_1^7 = p_r, \end{aligned} \tag{32}$$

with

$$\tilde{c}_T(A) = c_T(A, \tilde{\theta}(A)) \tag{33}$$

and

$$\tilde{\theta}(A) = \hat{\theta} + \frac{\hat{A} - A}{T}, \tag{34}$$

where $\hat{A}$ and $\hat{\theta}$ are reference values. Since Riemann invariants Γ_1^j with $j = 1,\dots,7$ are constant along ξ we have

$$\frac{d\Gamma_1^j(\xi)}{d\xi} = \nabla_{\tilde{\mathbf{Q}}}\Gamma_1^j(\xi)\cdot\frac{d\tilde{\mathbf{Q}}(\xi)}{d\xi} = 0, \tag{35}$$

which is equivalent to (20).

A similar procedure shows that Riemann invariants for characteristic fields associated to λ_8 are

$$\begin{aligned}
&\Gamma_8^1 = u - \int_{\hat{A}}^{A}\frac{\tilde{c}_T(\xi)}{\xi}d\xi, \quad \Gamma_8^2 = \theta + \frac{A}{T},\\
&\Gamma_8^3 = A_0, \quad \Gamma_8^4 = h_0, \quad \Gamma_8^5 = E_e,\\
&\Gamma_8^6 = E_c, \quad \Gamma_8^7 = p_r.
\end{aligned} \tag{36}$$

With regard to linearly degenerate fields, Riemann invariants for characteristic fields associated to λ_2 to λ_7 are

$$\Gamma_1^{LD} = p + \frac{1}{2}\rho u^2 = constant \tag{37}$$

and

$$\Gamma_2^{LD} = q = constant. \tag{38}$$

In fact, it can be easily verified that relations (37) and (38) satisfy the system of six PDEs

$$\nabla_{\mathbf{Q}}\Gamma_j^{LD}\cdot\mathbf{R}_k \equiv 0, \tag{39}$$

with $j = 1,2$ and $k = 2,3,\dots,7$. The fact of having two generalized Riemann invariants instead of seven is related to the similar structure of eigenvectors associated to λ_k with $k = 2,3,4,5,7$.

3. Numerical methods

Here we illustrate the numerical methodology used to solve the one-dimensional blood flow model (10), as well as the treatment of junctions. Moreover, we pay special attention to the treatment of junctions in order to preserve the formal order of accuracy of the numerical scheme.

It is important to note that the hyperbolization proposed in 2.2 has two important implications from the numerical point of view. First, the relaxation time T appears in (16), resulting in larger values of the celerity if compared to the elastic case. Second, the third component of source term (13) might be stiff for small values of T. Because of these two implications, the numerical scheme to be used must be efficient and must be able to treat stiff source terms appropriately. Here we use a finite-volume type path-conservative numerical scheme of high order of accuracy in space and time that has already showed to possess these abilities for hyperbolized one-dimensional blood flow models [31]. We present a brief summary of the above mentioned methods and references to more specific works addressing in detail these issues will be given in due course.

3.1. Finite-volume type numerical scheme

Here we present a brief summary of the numerical methodology used to solve system (10). Full details for the first-order scheme, as well as its high-order extension can be found in [40] and references therein.

3.1.1. Path-conservative finite-volume-type numerical scheme

Discretization of (10) by a path-conservative finite-volume type scheme yields

$$\mathbf{Q}_i^{n+1} = \mathbf{Q}_i^n - \frac{1}{\Delta x_i}\int_{t^n}^{t^{n+1}}\int_{x_{i-\frac{1}{2}}}^{x_{i+\frac{1}{2}}} \mathbf{A}(\mathbf{Q})\partial_x \mathbf{Q} dx dt - \frac{\Delta t^n}{\Delta x_i}\left(\mathbf{D}^-_{i+\frac{1}{2}} + \mathbf{D}^+_{i-\frac{1}{2}}\right) + \Delta t^n \mathbf{S}_i\,, \tag{40}$$

for $i = 1,\ldots,N$, where N is the number of computational cells, $\Delta x_i = x_{i+\frac{1}{2}} - x_{i-\frac{1}{2}}$ is the mesh spacing and $\Delta t^n = t^{n+1} - t^n$ is the time step. As for any finite-volume type scheme, we note that

$$\mathbf{Q}_i^n = \frac{1}{\Delta x_i}\int_{x_{i-\frac{1}{2}}}^{x_{i+\frac{1}{2}}} \mathbf{Q}(x,t^n)\,dx\,, \tag{41}$$

$$\mathbf{S}_i = \frac{1}{\Delta t^n \Delta x_i}\int_{t^n}^{t^{n+1}}\int_{x_{i-\frac{1}{2}}}^{x_{i+\frac{1}{2}}} \mathbf{S}(\mathbf{Q}(x,t))dx dt \tag{42}$$

and

$$\mathbf{D}^{\mp}_{i\pm\frac{1}{2}} = \frac{1}{\Delta t^n}\int_{t^n}^{t^{n+1}} \mathcal{D}^{\mp}_{i\pm\frac{1}{2}}\left(\mathbf{Q}^-_{i\pm\frac{1}{2}}(t), \mathbf{Q}^+_{i\pm\frac{1}{2}}(t), \Psi\right) dt\,. \tag{43}$$

Here $\mathbf{Q}^{\pm}_{i\pm\frac{1}{2}}(t)$ are accurate approximations of the sought solution for the time interval $t = [t^n, t^{n+1}]$ at both sides of the cell interface $x_{i\pm\frac{1}{2}}$ and $\mathcal{D}^{\mp}_{i\pm\frac{1}{2}}\left(\mathbf{Q}^-_{i\pm\frac{1}{2}}(t), \mathbf{Q}^+_{i\pm\frac{1}{2}}(t), \Psi\right)$ is a monotone first order fluctuation [41] defined as

$$\mathcal{D}^{\mp}_{i\pm\frac{1}{2}} = \frac{1}{2}\int_0^1 \left[\mathbf{A}(\Psi(\mathbf{Q}^-_{i\pm\frac{1}{2}}, \mathbf{Q}^+_{i\pm\frac{1}{2}}, s)) \mp |\mathbf{A}(\Psi(\mathbf{Q}^-_{i\pm\frac{1}{2}}, \mathbf{Q}^+_{i\pm\frac{1}{2}}, s))|\right] \frac{\partial \Psi}{\partial s} ds\,, \tag{44}$$

where the path $\Psi = \Psi(\mathbf{Q}^-, \mathbf{Q}^+, s)$, with $0 \le s \le 1$, is a Lipschitz continuous function that connects the left state $\mathbf{Q}^-$ to the right state $\mathbf{Q}^+$ in phase-space, satisfying

$$\Psi\left(\mathbf{Q}^-, \mathbf{Q}^+, 0\right) = \mathbf{Q}^-,\ \Psi\left(\mathbf{Q}^-, \mathbf{Q}^+, 1\right) = \mathbf{Q}^+\,. \tag{45}$$

Details on the computation of first order fluctuations can be found in [40] and references therein.

High-order accuracy in space and time is achieved by computing accurate space-time evolution of the state vector within the control volume $[x_{i-\frac{1}{2}}, x_{i+\frac{1}{2}}] \times [t^n, t^{n+1}]$ and time integrals along cell interfaces. This is achieved by adopting the Dumbser-Enaux-Toro (DET) solver, which was proposed in [42] and extended to non-conservative systems in [43, 44].

3.1.2. Spatial reconstruction

As many high-order finite volume solvers, the DET solver requires a spatial reconstruction procedure based on cell averages, which are the quantities actually evolved by the numerical scheme. As previously reported [32, 40], here we use the Weighted Essentially Non-Oscillatory (WENO) methodology proposed in [45] by which spatial polynomials over the entire computational cell are obtained. First we introduce reference coordinates $0 \le \xi \le 1$ given by $x = x_{i-\frac{1}{2}} + \xi \Delta x_i$. For a scheme of order p, at each time level t^n, we reconstruct element-wise polynomials of the type

$$\mathbf{w}_h = \mathbf{w}_h(\xi, t^n) = \sum_{l=1}^{M+1} \psi_l(\xi)\hat{\mathbf{w}}_l(t^n) := \psi_l(\xi)\hat{\mathbf{w}}_l(t^n), \tag{46}$$

where $M = p - 1$ is the polynomial degree of the spatial reconstruction, $\psi_l(\xi)$, $l = 1,\ldots,M+1$, are the corresponding basis functions and $\hat{\mathbf{w}}_l(t^n)$, $l = 1,\ldots,M+1$, are the expansion coefficients at

time $t = t^n$. Note that in (46) the Einstein summation convention was introduced and will be used throughout the rest of this work.

Details on the spatial reconstruction are omitted since the methodology is rather standard and was extensively documented in the literature. For details on the particular WENO version used in this paper see [45, 46]. We note that in the case of one-dimensional blood flow, there will be cells of certain stencils lying outside the physical domain. The treatment of spatial reconstruction in such situations was addressed in [32] and will be briefly illustrated in Section 3.3.

3.1.3. Space-time implicit discontinuous Galerkin prediction

In order to obtain an accurate prediction for the control volume $T_i = [x_{i-\frac{1}{2}}, x_{i+\frac{1}{2}}] \times [t^n, t^{n+1}]$, the DET solver relies on a space-time local Discontinuous-Galerkin (DG) scheme [42, 43, 44] which will provide a space-time polynomial $\mathbf{Q}_h$ to be later used to solve integrals in (40). After transforming system (10) to a reference space-time element $T_E = [0,1] \times [0,1]$ with reference coordinates ξ and τ, related to the physical domain by $x = x_{i-\frac{1}{2}} + \Delta x_i \, \xi$ and $t = t^n + \Delta t^n \, \tau$, we obtain

$$\partial_\tau \mathbf{Q}_h + \mathbf{A}^* \partial_\xi \mathbf{Q}_h = \mathbf{S}^* , \tag{47}$$

with

$$\mathbf{A}^* := \frac{\Delta t^n}{\Delta x_i} \mathbf{A}(\mathbf{Q}_h), \quad \mathbf{S}^* := \Delta t^n \mathbf{S}(\mathbf{Q}_h).$$

We multiply (47) by a space-time basis function $\phi = \phi(\xi, \tau)$, integrate over the reference element T_E and then use integration by parts for the time derivative term in order to obtain

$$[\phi, \mathbf{Q}_h]^1 - \langle \partial_\tau \phi, \mathbf{Q}_h \rangle_{T_E} + \langle \phi, \mathbf{A}^* \partial_\xi \mathbf{Q}_h \rangle_{T_E} = [\phi, \mathbf{w}_h]^0 + \langle \phi, \mathbf{S}^* \rangle_{T_E} , \tag{48}$$

where we have introduced the following operators to simplify notation

$$[a,b]^\tau = \int_0^1 a(\xi,\tau) b(\xi,\tau) d\xi , \quad \langle a,b \rangle_{T_E} = \int_0^1 \int_0^1 a(\xi,\tau) b(\xi,\tau) d\xi d\tau . \tag{49}$$

Next, by using the same space-time basis functions ϕ, to approximate $\mathbf{Q}_h$, $\mathbf{A}^* \partial_\xi \mathbf{Q}_h$ and $\mathbf{S}^*$, we obtain

$$\left([\phi_k, \phi_l]^1 - \langle \partial_\tau \phi_k, \phi_l \rangle_{T_E} \right) \hat{\mathbf{Q}}_l - \langle \phi_k, \phi_l \rangle_{T_E} \widehat{\mathbf{S}^*}_l = [\phi_k, \psi_l]^0 \hat{\mathbf{w}}_l - \langle \phi_k, \phi_l \rangle_{T_E} \widehat{\mathbf{A}^* \partial_\xi \mathbf{Q}}_l , \tag{50}$$

for $k = 1, 2, \ldots, (M+1)^2$.

Expansion coefficients $\hat{\mathbf{Q}}_l$ are obtained by a fixed point iteration procedure, see [42] for details, in which at each iteration step, $m = 0, 1, \ldots$ until convergence is achieved, we solve

$$\left([\phi_k, \phi_l]^1 - \langle \partial_\tau \phi_k, \phi_l \rangle_{T_E} \right) \hat{\mathbf{Q}}_l^{m+1} - \langle \phi_k, \phi_l \rangle_{T_E} \widehat{\mathbf{S}^*}_l^{m+1} = [\phi_k, \psi_l]^0 \hat{\mathbf{w}}_l - \langle \phi_k, \phi_l \rangle_{T_E} \widehat{\mathbf{A}^* \partial_\xi \mathbf{Q}}_l^m , \tag{51}$$

for $k = 1, 2, \ldots, (M+1)^2$. For full details the reader is referred to [42] for a general introduction to the DET solver and to [32, 40] for the implementation of the DET solver in the context of one-dimensional blood flow.

3.2. Treatment of viscoelastic junctions - Riemann problem at a junction

System (10) provides all the necessary information to set up an approximate Riemann solver at a junction. In the following we apply the methodology proposed in [32] to the system under study. The methodology makes use of standard knowledge on the solution of the Riemann problem. The reader is referred to [47] for background.

If we consider N_P vessels sharing a vertex, the Riemann problem at the vertex is defined as

$$\begin{cases} \partial_t \mathbf{Q}^k + \mathbf{A}(\mathbf{Q}^k)\partial_x \mathbf{Q}^k = 0\,, x \in \mathcal{R}\,, t > 0\,, \\ \mathbf{Q}^k(x,0) = \mathbf{Q}^k_{1D}\,, \end{cases} \tag{52}$$

for $k = 1,\ldots,N_P$.

The self-similar solution to (52) consists of $2N_P$ constant states, where N_P states are the initial condition states provided by the one-dimensional vessels $\mathbf{Q}^k_{1D}$, with $k = 1,\ldots,N_P$, while the remaining states $\mathbf{Q}^k_*$, with $k = 1,\ldots,N_P$, are states connected to initial condition states via non-linear waves and among themselves via the linearly degenerate stationary contact discontinuity. Wave relations linking the above mentioned states in phase space are given by generalized Riemann invariants (32), (36) and (37) and (38). Since system (10) can not be recast in conservative form [31], we choose to implement an approximate Riemann solver that only admits the formation of rarefactions. This kind of approximate solvers has been widely applied and demonstrated to be robust and accurate [47]. An interesting feature of this solver is that it is exact if all non-linear waves happen to be rarefactions.

The unknown state vectors $\mathbf{Q}^k_*\,, k = 1,\ldots,N_P$ are computed by solving the following non-linear system of $3N_P$ equations

$$\begin{cases} \sum\limits_{k=1}^{N_P} g^k_P A^k_* u^k_* = 0\,, \\ p(A^1_*,\theta^1_*) + \dfrac{1}{2}\rho(u^1_*)^2 - p(A^k_*,\theta^k_*) - \dfrac{1}{2}\rho(u^k_*)^2 = 0, \;\; k = 2,\ldots,N_P\,, \\ u^k_* - u^k_{1D} + g^k_P \beta^k = 0\,, \;\; k = 1,\ldots,N_P\,, \\ \theta^k_* + \dfrac{A^k_*}{T^k} - \theta^k_{1D} - \dfrac{A^k_{1D}}{T^k} = 0\,, \;\; k = 1,\ldots,N_P\,. \end{cases} \tag{53}$$

Here, β^k is

$$\beta^k = \int_{A^k_{1D}}^{A^k_*} \frac{\tilde{c}_T(\xi)}{\xi} d\xi \tag{54}$$

and g^k_P is the auxiliary function

$$g^k_P = \begin{cases} 1\,, & \text{if } x^k_P = L^k\,, \\ -1\,, & \text{if } x^k_P = 0\,, \end{cases} \tag{55}$$

where x^k_P is the local coordinate of the k-th vessel, evaluated at vertex P and L^k is the vessel length. Note that we have allowed T to be different for each vessel. This does not alter the eigenstructure analysis performed in Section 2 and is only relevant for junctions, since we assume $T = constant$ within each vessel.

3.3. Ghost cell filling for spatial reconstruction

The issue of how to deal with the spatial reconstruction at cells for which stencils lay outside the physical domain was addressed by the authors in [32]. Here we propose an improved version of the data extrapolation step in which the interaction between vessels sharing a vertex is taken into account for both the leading term and the spatial derivatives of the Taylor series expansion.

At time t^n, the WENO procedure requires the state variable value at M ghost cells at each side of the one-dimensional edge. Therefore, an accurate approximation of the solution is required in

order to compute cell averages that will then be used to fill ghost cells. Here, the approximation used to compute cell averages is provided by a Taylor series expansion around the internal vertex P, shared by the k-th edge. Assuming that the origin of a local spatial coordinate ε is located at the internal vertex P, shared by the k-th edge, the state vector outside the one-dimensional domain for this edge has the form

$$\mathbf{Q}_g^k(\varepsilon, t^n) = \mathbf{Q}_*^k(t^{n-1} + \Delta t^{n-1}) + \sum_{j=1}^{M} \frac{1}{j!} \partial_x^{(j)} \mathbf{Q}_*^k(t^{n-1} + \Delta t^{n-1})\, \varepsilon^j \,, \tag{56}$$

where $\mathbf{Q}_*^k(t^{n-1} + \Delta t^{n-1})$ is the solution of the Riemann problem at a junction (52) for initial conditions given by the prediction of the DET solver, obtained in the previous time step. For the case $n = 0$, the initial condition is used to assign $\mathbf{Q}_*^k(t^{n-1} + \Delta t^{n-1})$ and its spatial derivatives.

In order to compute the spatial derivatives needed in (56), we apply a procedure used in the Tiratev-Toro generalized Riemann problem solver [48, 49]. According to the Toro-Titarev solver, spatial derivatives are computed from a linearized version of the original PDE system. The linearization is performed around the solution to a classical Riemann problem. Therefore, we compute $\partial_x^{(j)} \mathbf{Q}_*^k(t^{n-1} + \Delta t^{n-1})$, by solving a Riemann problem at the junction for a linearized system

$$\begin{cases} \partial_t(\partial_x^{(j)} \mathbf{Q}^k(t^{n-1} + \Delta t^{n-1})) + \bar{\mathbf{A}}^k \partial_x(\partial_x^{(j)} \mathbf{Q}^k(t^{n-1} + \Delta t^{n-1})) = 0 \,, x \in \Re \,, t > 0 \,, \\ \partial_x^{(j)} \mathbf{Q}^k(t^{n-1} + \Delta t^{n-1}) = \partial_x^{(j)} \mathbf{Q}_{1D}^k(t^{n-1} + \Delta t^{n-1}) \,, \end{cases} \tag{57}$$

for $k = 1, \ldots, N_P$. In (57), $\bar{\mathbf{A}}^k$ is the linearized Jacobian

$$\bar{\mathbf{A}}^k = \mathbf{A}(\mathbf{Q}_*^k(t^{n-1} + \Delta t^{n-1})) \,.$$

Initial conditions for spatial derivatives needed in (57) are directly taken from the implict DG prediction of the previous time step by recursively making the following *ansatz*

$$\langle \theta_k, \theta_l \rangle \widehat{\partial_\xi^{(j)} \mathbf{Q}}_l = \langle \theta_k, \partial_\xi \theta_l \rangle \widehat{\partial_\xi^{(j-1)} \mathbf{Q}}_l \,, \tag{58}$$

with $j = 1, \ldots, M$ and $k, l = 1, 2, \ldots, (M+1)^2$. Note that matrix $\langle \theta_k, \theta_l \rangle^{-1} \langle \theta_k, \partial_\xi \theta_l \rangle$ is computed only once, so that the spatial derivatives are obtained by a simple matrix-vector product. It is worth noting that the computational cost of solving the Riemann problem for the linearized system is rather modest and amounts to solving M linear systems of $3N_P$. For example, for a second order scheme, only one linear system has to be solved.

3.4. Treatment of other boundary conditions

Additional boundary conditions have to be assigned to a network of one-dimensional vessels. In particular, one might have to prescribe pressure or flow rate at a given location (the inflow at the root of the aorta is perhaps the most remarkable example), or couple terminal vessels to lumped parameter models. Usually, the prescribed quantity regards only one component of state vector (11). In all cases the constancy of Riemann invariants across rarefaction waves is used to determine the value of the missing state variables. Since system (10) considers the auxiliary variable θ, no assumption on $\partial_x q$ has to be made in correspondence of any kind of boundary condition, since wave relations (32) will naturally deliver this quantity. The treatment of boundary conditions is not trivial since we are dealing with a non-conservative system. Therefore the reader is referred to [32] for further details on the assignment of boundary conditions in the context of the proposed methodology.

3.5. Alternative method: operator splitting

In order to compare the computational results obtained by applying the proposed methodology with results obtained using widely applied methods for one-dimensional blood flow in vessels with viscoelastic walls, we have implemented the operator splitting technique, which is one of the alternatives found in the specialized literature [26, 36]. We split the problem into a hyperbolic and a parabolic problem by noting that one can write

$$\zeta(x,t) = \zeta_{\text{elas}}(x,t) + \zeta_{\text{visco}}(x,t), \tag{59}$$

where

$$\zeta_{\text{elas}}(x,t) = \frac{\pi R_0 h_0}{A_d}\left[E_e\varepsilon + E_c\epsilon_r \ln(e^{\chi}+1)\right] \tag{60}$$

and

$$\zeta_{\text{visco}}(x,t) = -\frac{\pi R_0 h_0}{A_d}\left[\frac{K_m}{2\sqrt{AA_0}}\partial_x q\right]. \tag{61}$$

Replacing (59) in (1) and taking into account the spatial variation of mechanical and geometrical properties of the vessel, as done for system (10), we obtain

$$\partial_t \mathbf{W} + \mathbf{A}_{\text{elas}}(\mathbf{W})\partial_x \mathbf{W} = \mathbf{S}_{\text{elas}}(\mathbf{W}) + \mathbf{S}_{\text{visco}}(\mathbf{W}, \partial_x^2 \mathbf{W}), \tag{62}$$

where

$$\mathbf{W} = [A, q, A_0, h_0, E_e, E_c, p_r]^T,$$

$$\mathbf{S}_{\text{elas}}(\mathbf{W}) = [0, f, 0, 0, 0, 0, F]$$

and

$$\mathbf{S}_{\text{visco}}(\mathbf{W}, \partial_x^2 \mathbf{W}) = [0, C\partial_x^2 q, 0, 0, 0, 0, 0]^T,$$

where C will depend on the choice for A_d in (61). The Jacobian $\mathbf{A}_{\text{elas}}(\mathbf{W})$ is not reported here for the sake of brevity.

A first order operator splitting allows us to separate the advection-diffusion-reaction problem into a convective and a diffusive subproblem. The discrete analogue of the splitting scheme results in

$$\left.\begin{aligned} PDEs: &\quad \partial_t \mathbf{W} + \mathbf{A}_{\text{elas}}(\mathbf{W})\partial_x \mathbf{W} = \mathbf{S}_{\text{elas}}(\mathbf{W}), \\ IC: &\quad \mathbf{W}(x,t^n) = \mathbf{W}_h^n, \end{aligned}\right\} \rightarrow \overline{\mathbf{W}}_h^{n+1}, \tag{63}$$

and

$$\left.\begin{aligned} PDEs: &\quad \partial_t \mathbf{W} = \mathbf{S}_{\text{visco}}(\mathbf{W}, \partial_x^2 \mathbf{W}), \\ IC: &\quad \mathbf{W}(x,t^n) = \overline{\mathbf{W}}_h^{n+1}, \end{aligned}\right\} \rightarrow \mathbf{W}_h^{n+1}, \tag{64}$$

where $\overline{\mathbf{W}}_h^{n+1}$ is an intermediate state, given by the approximation of the solution to the hyperbolic subproblem and $\mathbf{W}_h^{n+1}$ is the numerical approximation of $\mathbf{W}$ at time t^{n+1}. The hyperbolic subproblem is solved with a first order version of the path-conservative scheme proposed in Section 3.1, whereas the correction step is performed by discretizing the resulting parabolic equation using centered finite differences and backward Euler for the spatial and time discretization, respectively. For details on the operator splitting technique see [47], for example. As reported in the literature [26, 28], at the edges of vessels we impose homogeneous Neumann boundary conditions for the flow.

It is important to note that imposing homogeneous Neumann conditions for the flow gradient is equivalent to neglecting the contribution of viscoelastic properties of the vessel wall to the momentum balance equation at vessel edges. As discussed in Section 1, this is exactly what is done

by most practitioners, even if the terms derived from the viscoelastic character of vessel walls is treated differently from what is reported here. Therefore one might expect that, if different approaches are consistent, the effect observed in the numerical results by considering one technique or the other should be similar, as long as viscoelasticity is neglected at junctions.

4. Results

We present a set of numerical tests to validate the proposed coupling strategy. Tests regard a convergence test, academic tests in simple vessel networks and the application of the proposed methodology to one-dimensional blood flow in a simple and an anatomically detailed arterial networks.

4.1. Convergence rates

We perform a convergence study in order to verify that the expected theoretical order of accuracy of the proposed numerical scheme is reached. We consider a smooth function

$$\hat{\mathbf{Q}}(x,t) = \begin{bmatrix} \hat{A}(x,t) \\ \hat{q}(x,t) \end{bmatrix} = \begin{bmatrix} A^c + \delta_A A^c \sin\left(\frac{2\pi}{L}x\right)\cos\left(\frac{2\pi}{T_0}t\right) \\ q^c - \delta_A A^c \frac{L}{T_0}\cos\left(\frac{2\pi}{L}x\right)\sin\left(\frac{2\pi}{T_0}t\right) \end{bmatrix}, \tag{65}$$

where quantities with superscript c are average values and terms δ are fluctuations around the average. We then perform the convergence tests by solving a modification of (10), namely

$$\partial_t \mathbf{Q} + \mathbf{A}(\mathbf{Q})\partial_x \mathbf{Q} = \mathbf{S}(\mathbf{Q}) + \hat{\mathbf{S}}(x,t), \tag{66}$$

where $\hat{\mathbf{S}}(x,t)$ contains non-zero terms resulting from replacing (65) in (1). Note that (65) is replaced in the original system and not in the hyperbolized one, so that the only non-zero component of $\hat{\mathbf{S}}(x,t)$ regards the momentum balance equation.

The convergence test is performed over a network composed by two vessels connected at both extremities, thus forming a closed loop. Reference parameters are: $h = 0.5\,mm$, $R_0 = 14\,mm$, $E_E = 1.2\,MPa$, $2/3 K_m h_0\sqrt{\pi} = 1\,Pa s m$ $p_0 = 0\,Pa$, $\mu = 0\,Pa\,s$ and $\hat{A} = 3/4\,A_0$. Moreover, the following parameters are used: $L = 1\,m$, $T_0 = 1\,s$, $A^c = \pi R_0^2$, $\delta_A = 0.1$, $q^c = 100\,ml\,s^{-1}$. The output time is taken as $t_{\text{end}} = 0.5\,s$ and the CFL number used is $CFL = 0.9$. Errors for the three state variables of interest, *i.e.* A, q and θ, were measured in the norms L^1, L^2 and L^∞.

Tables 1 and 3 display the empirical convergence rates for second and third order versions of the proposed finite volume-type numerical scheme, respectively. The relaxation time used in both cases was $T = 10^{-3}\,s$. The expected convergence rate for all quantities is achieved, including the auxiliary variable θ that stands for the gradient of flow rate. Moreover, Tables 2 and 4 show convergence rates for the case in which T is chosen so that $\triangle = 1$. Also in this case the convergence for area and flow rate is achieved. As expected, convergence rates for θ differ from the expected order of accuracy, since in this particular test we are changing the mathematical model at each refinement step (T is different for each mesh), making the computation of convergence rates for this quantity unfeasible. However, we note that errors are always lower than or equal to the ones obtained using a fixed relaxation time, see Tables 1 and 3.

4.2. Simple networks

In order to explore the effect of performing a proper coupling of viscoelastic vessels, we first consider two simple vessel networks. Geometrical and mechanical properties of vessels composing both networks are shown Table 5. Other relevant parameters are: $\mu = 0\,Pa\,s$; $\rho = 1050\,kg\,m^{-3}$, $E_c = 0$ and $\hat{A} = 3/4\,A_0$. A CFL number of $CFL = 0.9$ and a relaxation time T that ensures that

Var.	N	L^1	L^2	L^∞	$\mathcal{O}(L^1)$	$\mathcal{O}(L^2)$	$\mathcal{O}(L^\infty)$	Δ
$A[cm^2]$	4	2.53e-02	3.05e-02	7.35e-02	-	-	-	
	8	5.91e-03	7.36e-03	2.09e-02	2.1	2.1	1.8	1.03e-02
	16	1.41e-03	1.77e-03	5.14e-03	2.1	2.1	2.0	4.10e-02
	32	3.35e-04	4.29e-04	1.36e-03	2.1	2.0	1.9	1.64e-01
	64	8.11e-05	1.05e-04	3.47e-04	2.0	2.0	2.0	6.56e-01
$q[cm^3/s]$	4	2.17e+00	2.17e+00	2.24e+00	-	-	-	
	8	6.33e-01	8.51e-01	1.32e+00	1.8	1.3	0.8	1.03e-02
	16	2.09e-01	2.46e-01	4.64e-01	1.6	1.8	1.5	4.10e-02
	32	4.88e-02	5.33e-02	1.09e-01	2.1	2.2	2.1	1.64e-01
	64	1.15e-02	1.24e-02	2.88e-02	2.1	2.1	1.9	6.56e-01
$\theta[cm^2/s]$	4	9.75e+00	9.82e+00	1.08e+01	-	-	-	
	8	3.57e+00	4.02e+00	5.41e+00	1.4	1.3	1.0	1.03e-02
	16	4.85e-01	5.93e-01	1.01e+00	2.9	2.8	2.4	4.10e-02
	32	1.01e-01	1.20e-01	2.25e-01	2.3	2.3	2.2	1.64e-01
	64	2.14e-02	2.53e-02	5.38e-02	2.2	2.3	2.1	6.56e-01

Table 1: Empirical convergence rates obtained for a second order implementation of the numerical scheme and $T = 1e-3$. N is the number of cells and Δ is defined in (8).

Var.	N	L^1	L^2	L^∞	$\mathcal{O}(L^1)$	$\mathcal{O}(L^2)$	$\mathcal{O}(L^\infty)$	Δ
$A[cm^2]$	4	2.53e-02	3.13e-02	7.21e-02	-	-	-	
	8	6.41e-03	7.48e-03	1.90e-02	2.0	2.1	1.9	1.00e+00
	16	1.46e-03	1.82e-03	5.21e-03	2.1	2.0	1.9	1.00e+00
	32	3.35e-04	4.28e-04	1.34e-03	2.1	2.1	2.0	1.00e+00
	64	8.10e-05	1.05e-04	3.41e-04	2.0	2.0	2.0	1.00e+00
$q[cm^3/s]$	4	3.31e+00	3.33e+00	3.76e+00	-	-	-	
	8	9.93e-01	1.28e+00	2.08e+00	1.7	1.4	0.9	1.00e+00
	16	2.53e-01	3.32e-01	6.83e-01	2.0	2.0	1.6	1.00e+00
	32	5.19e-02	5.78e-02	1.16e-01	2.3	2.5	2.6	1.00e+00
	64	1.13e-02	1.18e-02	2.11e-02	2.2	2.3	2.5	1.00e+00
$\theta[cm^2/s]$	4	2.06e-01	2.06e-01	2.13e-01	-	-	-	
	8	1.70e-01	1.83e-01	2.36e-01	0.3	0.2	-0.2	1.00e+00
	16	4.05e-02	4.33e-02	5.90e-02	2.1	2.1	2.0	1.00e+00
	32	1.40e-02	1.75e-02	3.50e-02	1.5	1.3	0.8	1.00e+00
	64	2.18e-02	2.47e-02	4.07e-02	-0.6	-0.5	-0.2	1.00e+00

Table 2: Empirical convergence rates obtained for a second order implementation of the numerical scheme and adaptive T so that $\Delta = 1$ for each mesh. N is the number of cells and Δ is defined in (8).

$\Delta = 1$ were used for all computations reported in this section. The following flow is prescribed at the network inlet

$$q_{bc} = \hat{q}\, e^{-10000(t-0.025)^2}, \tag{67}$$

where $\hat{q} = 100\, ml\, s^{-1}$. Moreover, absorbing boundary conditions are considered for outlets of terminal vessels. Mesh size for solutions obtained using the proposed methodology is $\Delta x = 10\, mm$ for all tests, unless otherwise indicated. In turn, the mesh size for solutions obtained by the operator splitting technique is $\Delta x = 1\, mm$. Numerical solutions obtained using the proposed methodology will be denoted as *JVIS-Op*, where p is the order of accuracy of the scheme, while numerical solutions obtained with the operator splitting technique will be denoted as *SPLIT*. This notation will be maintained throughout the rest of the manuscript.

4.2.1. Test 1: two vessels network

In this case the network is composed by two vessels with identical properties, namely vessels V2 and V3 of Table 5. This is the simplest test one could think of and a reference solution is obtained by solving the equivalent problem (same boundary conditions) for vessel V1. Any differences between the solutions obtained for vessel V1 and for the network (given by vessels V2-V3)

Var.	N	L^1	L^2	L^∞	$\mathcal{O}(L^1)$	$\mathcal{O}(L^2)$	$\mathcal{O}(L^\infty)$	Δ
$A[cm^2]$	4	1.07e-02	1.22e-02	2.31e-02	-	-	-	
	8	1.41e-03	1.75e-03	3.78e-03	2.9	2.8	2.6	3.22e-02
	16	1.83e-04	2.31e-04	5.79e-04	2.9	2.9	2.7	2.58e-01
	32	2.34e-05	2.91e-05	7.02e-05	3.0	3.0	3.0	2.06e+00
	64	3.80e-06	4.43e-06	1.00e-05	2.6	2.7	2.8	1.65e+01
$q[cm^3/s]$	4	3.06e+00	3.19e+00	4.12e+00	-	-	-	
	8	2.88e-01	3.18e-01	4.59e-01	3.4	3.3	3.2	3.22e-02
	16	2.48e-02	2.75e-02	4.02e-02	3.5	3.5	3.5	2.58e-01
	32	1.99e-03	2.21e-03	3.27e-03	3.6	3.6	3.6	2.06e+00
	64	6.60e-04	7.33e-04	1.04e-03	1.6	1.6	1.7	1.65e+01
$\theta[cm^2/s]$	4	1.20e+00	1.49e+00	3.07e+00	-	-	-	
	8	3.46e-01	3.87e-01	5.93e-01	1.8	1.9	2.4	3.22e-02
	16	1.90e-02	2.08e-02	3.51e-02	4.2	4.2	4.1	2.58e-01
	32	1.61e-03	1.77e-03	4.36e-03	3.6	3.6	3.0	2.06e+00
	64	2.40e-03	2.66e-03	3.76e-03	-0.6	-0.6	0.2	1.65e+01

Table 3: Empirical convergence rates obtained for a third order implementation of the numerical scheme and $T = 1e-3$. N is the number of cells and Δ is defined in (8).

Var.	N	L^1	L^2	L^∞	$\mathcal{O}(L^1)$	$\mathcal{O}(L^2)$	$\mathcal{O}(L^\infty)$	Δ
$A[cm^2]$	4	1.12e-02	1.25e-02	2.09e-02	-	-	-	
	8	1.60e-03	1.93e-03	4.00e-03	2.8	2.7	2.4	1.00e+00
	16	1.87e-04	2.33e-04	5.20e-04	3.1	3.1	2.9	1.00e+00
	32	2.30e-05	2.90e-05	7.90e-05	3.0	3.0	2.7	1.00e+00
	64	2.90e-06	3.70e-06	1.30e-05	3.0	3.0	2.6	1.00e+00
$q[cm^3/s]$	4	1.03e+00	1.09e+00	1.46e+00	-	-	-	
	8	1.70e-01	1.90e-01	2.73e-01	2.6	2.5	2.4	1.00e+00
	16	1.60e-02	1.78e-02	2.65e-02	3.4	3.4	3.4	1.00e+00
	32	2.57e-03	2.84e-03	4.18e-03	2.6	2.6	2.7	1.00e+00
	64	3.58e-04	3.99e-04	6.18e-04	2.8	2.8	2.8	1.00e+00
$\theta[cm^2/s]$	4	1.99e-01	2.08e-01	2.66e-01	-	-	-	
	8	5.10e-02	5.70e-02	8.14e-02	2.0	1.9	1.7	1.00e+00
	16	1.99e-03	2.34e-03	5.36e-03	4.7	4.6	3.9	1.00e+00
	32	1.02e-03	2.23e-03	9.59e-03	1.0	0.1	-0.8	1.00e+00
	64	1.38e-04	5.14e-04	3.29e-03	2.9	2.1	1.5	1.00e+00

Table 4: Empirical convergence rates obtained for a third order implementation of the numerical scheme and adaptive T so that $\Delta = 1$ for each mesh. N is the number of cells and Δ is defined in (8).

would be caused by an inconsistent coupling strategy.

Figure 1 shows computational results for pressure along the vessel network obtained with both, a second order implementation of the proposed methodology and the operator splitting technique at three time instants. The solution obtained with the coupling presented in this work is in perfect agreement with the solution obtained solving the same problem in the single vessel. On the other hand, the solution obtained using the operator splitting technique does not match the single vessel solution, also obtained using the operator splitting technique. The L^∞-norm of the difference between solutions obtained using one vessel or the two-vessel network are shown in Table 6. As expected, differences for the operator splitting technique are higher than those for the proposed methodology. In the latter case, differences for flow rate are of the order of magnitude of the L^∞ convergence test error for similar mesh sizes, see row for $N = 64$ in Table 1, so that differences can be attributed to the fact that at junctions we use a different reconstruction procedure and numerical flux, preserving however the order of accuracy. Clearly, errors differences for the operator splitting technique are above the ones obtained for the convergence test. Results not shown here, in which we use the hyperbolic reformulated system (10) and couple vessels setting $K_m = 0$ only in the resolution of the Riemann problem at the junction, *i.e.* neglecting the viscoelas-

Vessel name	$L[cm]$	$R_0[cm]$	$E_e[Pa]$	$h_0[cm]$	$2/3K_m h_0\sqrt{\pi}[Pasm]$
V1	40	1	1.2e+06	0.05	1.0
V2	20	1	1.2e+06	0.05	1.0
V3	20	1	1.2e+06	0.05	1.0
V4	20	0.1	1.2e+06	0.005	3.0

Table 5: Parameters for vessel network used in Section 4.2.

ticity only at the junctions, are similar to the ones obtained with the operator splitting technique. This observation is valid for all tests presented in this work. Moreover, it is worth noting that even if differences are small, and an inflow of short wave length was used, in the next sections we will show that these *junction effects* will have an impact on solutions obtained for relevant applications. Figure 2 shows computational results of pressure along the vessel network for a third order implementation of the proposed methodology. The improvement of the agreement of this solution and the reference solution is easily observable.

In order to exaggerate the effect of neglecting viscoelasticity at junctions, we perform the same test but now we increase the viscosity of the vessel wall by a factor of 5 in the entire network. Results for this test are shown in Figure 3. As expected, now the mismatch between the single vessel solution and the one including the junction is more evident. Moreover, we note that the solution obtained using the operator splitting technique presents *junction effects* also at the inlet of the network, whereas in the case of the proposed methodology the boundary conditions can be applied in a fully consistent manner, as explained in Section 3.4. We can also note that the mismatch between the results obtained using the proposed methodology and the reference solution is bigger than in the case where vessels were less viscoelastic (see Figure 1). This is due to the discretization error of the computational results. In fact, as shown in Figure 4, using a third order implementation of the proposed methodology, the numerical results approach the reference solution.

		$t = 0.036s$		$t = 0.052s$		$t = 0.068s$	
Value	Units	*JVIS-O2*	*SPLIT*	*JVIS-O2*	*SPLIT*	*JVIS-O2*	*SPLIT*
$\|\delta p\|_{L^\infty}$	$[Pa]$	0.10	7.10	0.70	8.40	0.20	14.00
$\|\delta q\|_{L^\infty}$	$[ml/s]$	0.01	0.58	0.02	0.35	0.01	0.65

Table 6: L^∞ norms for pressure and flow differences between one- and two-vessel numerical solutions at different times, referring to spatial plots of numerical results shown in Figure 1. *JVIS-O2*: second order implementation of the proposed methodology. *SPLIT*: operator splitting.

4.2.2. Test 2: three vessels

In this test we intend to resemble a physiologically relevant situation in which a small vessel (featuring high viscoelasticity) leaves a large vessel (with low viscoelasticity). This case is particularly relevant for perforator arteries that leave larger arteries as one moves distally (with respect to the heart). The network is now composed by vessels V2 (parent), V3 (daughter) and V4 (daughter). Vessel V4 is thrice as viscoelastic as the parent vessel and has radius and wall thickness ten times smaller.

Figures 5 and 6 show pressure along vessels V2-V3 and V2-V4, respectively. While the solution obtained using the operator splitting technique shows perturbations in correspondence to the junction which are not in agreement with the physics of the model, the pressure profile obtained with a second order version of the proposed methodology shows a smooth passage of the pressure wave

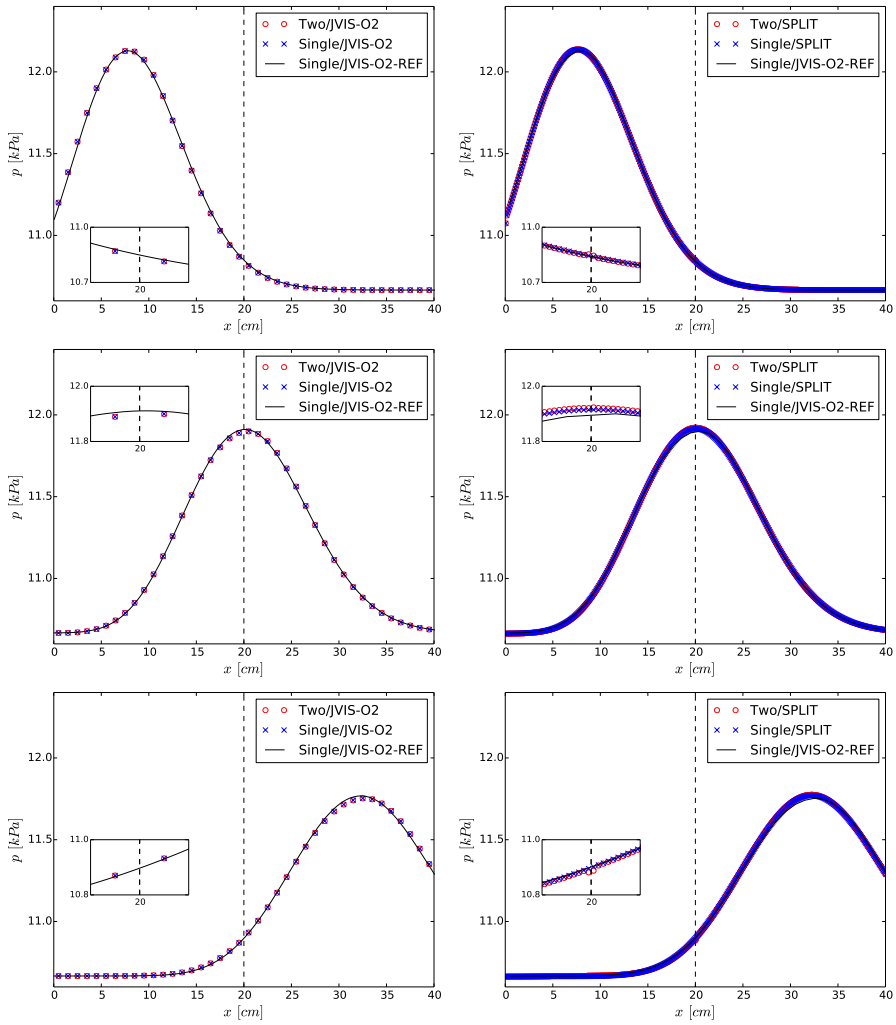

Figure 1: Test 1: pressure along vessels V2 and V3 for a second order implementation of the proposed strategy (left) and the operator splitting technique (right). *Two*: solution for vessel network; *Single*: solution for equivalent vessel; *JVIS-O2*: solution obtained with a second order implementation of the proposed methodology; *SPLIT*: solution obtained with the operator splitting technique; *JVIS-O2-REF*: solution obtained using the proposed methodology and $\Delta x_{\text{Ref}} = 1\,mm$ for the single vessel. Solution taken at $t = 0.036\,s$ (top row), $t = 0.052\,s$ (middle row) and $t = 0.068\,s$ (bottom row). Insets display the solution at the junction, whose location is depicted by the vertical dashed line.

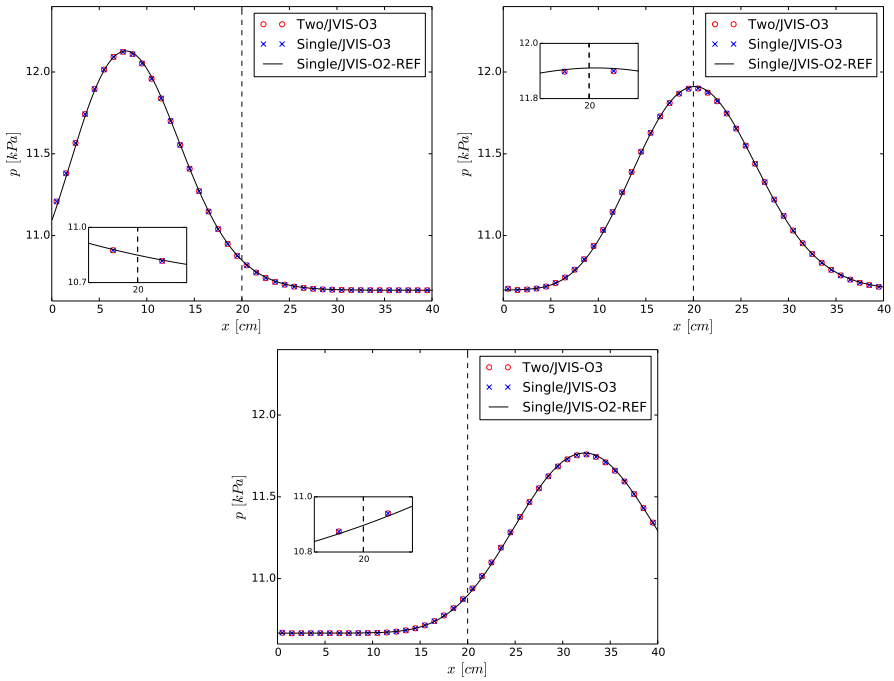

Figure 2: Test 1: pressure along vessels V2 and V3 for a third order implementation of the proposed strategy. *Two*: solution for vessel network; *Single*: solution for equivalent vessel; *JVIS-O3*: solution obtained with a third order implementation of the proposed methodology; *JVIS-O2-REF*: solution obtained using the proposed methodology and $\Delta x_{\text{Ref}} = 1\,mm$ for the single vessel. Solution taken at $t = 0.036\,s$ (top row), $t = 0.052\,s$ (middle row) and $t = 0.068\,s$ (bottom row). Insets display the solution at the junction, whose location is depicted by the vertical dashed line.

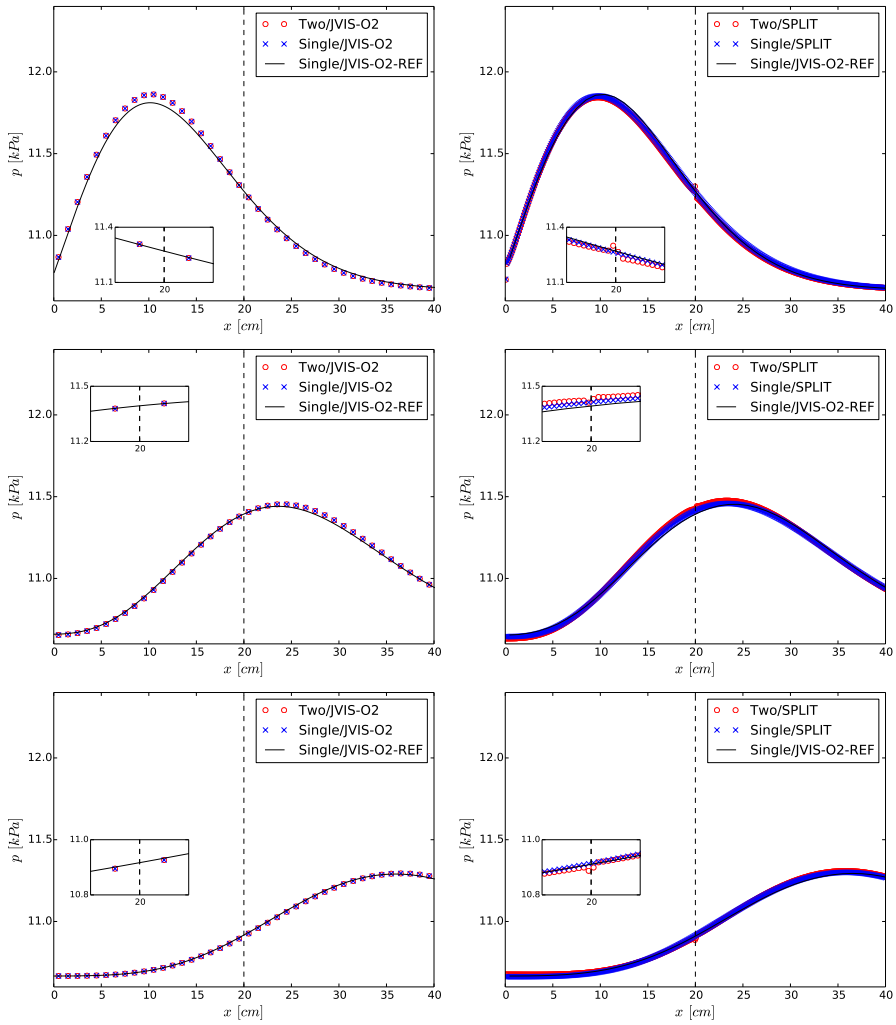

Figure 3: Test 1 (modified): Pressure along vessels V2 and V3 with $K_m^* = 5K_m$ for a second order implementation of the proposed strategy (left) and the operator splitting technique (right). *Two*: solution for vessel network; *Single*: solution for single vessel; *JVIS-O2*: solution obtained with a second order implementation of the proposed methodology; *SPLIT*: solution obtained with the operator splitting technique; *JVIS-O2-REF*: solution obtained using the proposed methodology and $\Delta x_{\text{Ref}} = 1mm$ for the single vessel. Solution taken at $t = 0.036s$ (top row), $t = 0.052s$ (middle row) and $t = 0.068s$ (bottom row). Insets display the solution at the junction, whose location is depicted by the vertical dashed line.

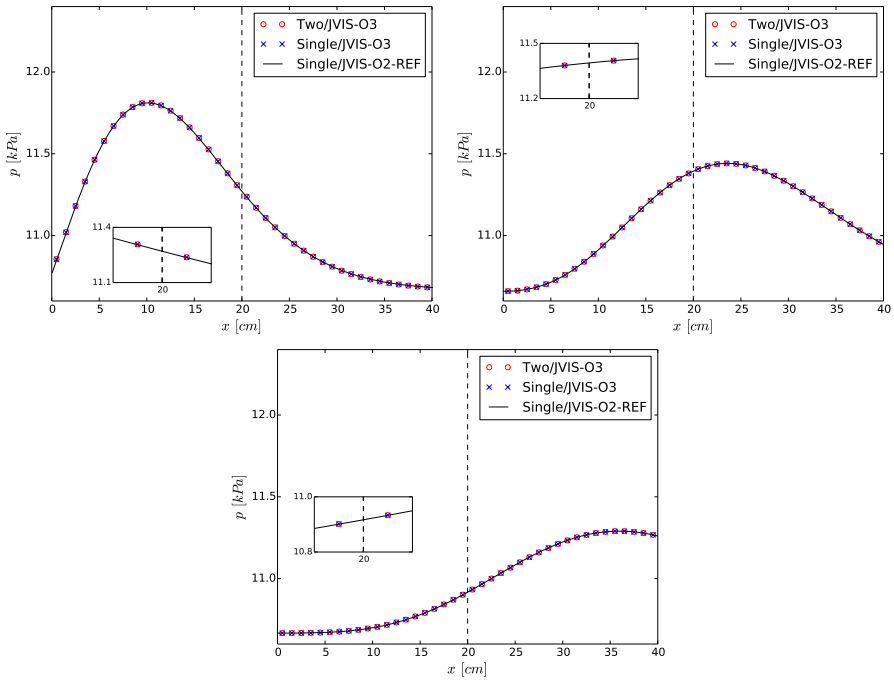

Figure 4: Test 1 (modified): Pressure along vessels V2 and V3 with $K_m^* = 5K_m$ for a third order implementation of the proposed strategy. *Two*: solution for vessel network; *Single*: solution for single vessel; *JVIS-O3*: solution obtained with a third order implementation of the proposed methodology; *JVIS-O2-REF*: solution obtained using the proposed methodology and $\Delta x_{\text{Ref}} = 1\,mm$ for the single vessel. Solution taken at $t = 0.036\,s$ (top row), $t = 0.052\,s$ (middle row) and $t = 0.068\,s$ (bottom row). Insets display the solution at the junction, whose location is depicted by the vertical dashed line.

across the junction. Computational results for a third order version of the proposed methodology are shown in Figures 8 and 7.

4.3. In vitro arterial network model

In order to assess the performance of the proposed methodology on a network of viscoelastic vessels, we consider the *in vitro* model of the human arterial system presented in [33] and further studied in [25]. The model includes 37 major arteries, an inflow curve at the root of the aorta and terminal resistances. A schematic representation of the network is shown in Figure 9. For full details on the model see [33] and [25]. The characteristic mesh size for solutions reported here is $\Delta x = 20\,mm$ for the proposed methodology and $\Delta x = 1\,mm$ for the operator splitting technique, whereas the reference solution was obtained using $\Delta x_{\text{Ref}} = 5\,mm$ and the proposed methodology. For the operator splitting approach, a minimum of three computational cells per vessel was used, whereas in the case of the proposed methodology the minimum number of cells per vessel was set to one. A $CFL = 0.9$ was used. The relaxation time was allowed to be different in each vessel, in order to guarantee that $\triangle = 1$ everywhere in the network. Results for the proposed methodology regard a second order implementation for which the average time step during the simulation was $\Delta t \approx 300\,\mu s$. Note that the time step is computed adaptively at each time iteration.

Figure 10 shows computational results for pressure and flow rate over a cardiac cycle at the midpoint of selected vessels. Differences between solutions obtained by the operator splitting method and the proposed methodology seem to be rather small. However, when looking at the spatial plots for pressure along the aorta and lower limb, reported in Figure 11, the effect of neglecting viscoelasticity at junctions becomes more evident than in the case of the time-pressure plots shown in Figure 10. In fact, it can be easily appreciated how the proposed methodology shows rather smooth transitions in pressure between different vessels, whereas the solution obtained by the operator splitting technique shows non-physical jumps across junctions. Of course small jumps are expected (see solution at $x = 80\,cm$), and indeed shown by the solutions obtained with the proposed methodology, but these have to be small since in this network $p >> \frac{1}{2}\rho u^2$. In other words, when not treating viscoelasticity properly in the formulation, the numerical results can display physical inconsistency at junctions. In turn, these inconsistencies will have an impact on the solution in the entire spatial domain.

4.4. Anatomically detailed upper limb vasculature

We consider the anatomically detailed arterial network of the arm presented in [34]. This network is part of the Anatomically Detailed Arterial Network (ADAN) model [12, 13]. The upper limb network comprises 201 arterial segments, spanning large, medium, small and even perforator arteries (see Figure 12). For a detailed description of the network topology, as well as its geometrical and mechanical parameters, refer to [12]. Of particular importance for the present study is the wide range of radii present in the network ($0.0235\,cm \leq R_0 \leq 0.2077\,cm$). As a result of the model parametrization strategy adopted for the ADAN model, this variability in radii implies that at certain junctions vessels with low viscoelastic properties (large radii) will connect to vessels with high viscoelastic properties (small radii). This is specially relevant in the case of small perforator arteries that are located along larger arteries in order to gradually feed vascular territories with the appropriate amount of blood. Briefly, vessel viscoelasticity in the ADAN model is defined as $K_m = W_m K_M$, where $K_M = 3000 Pa\,s$ and

$$W_m = \begin{cases} 0.001, & R_0 > 0.18\,cm, \\ 0.05, & 0.07\,cm \leq R_0 \leq 0.18\,cm, \\ 0.55, & R_0 < 0.07\,cm. \end{cases} \tag{68}$$

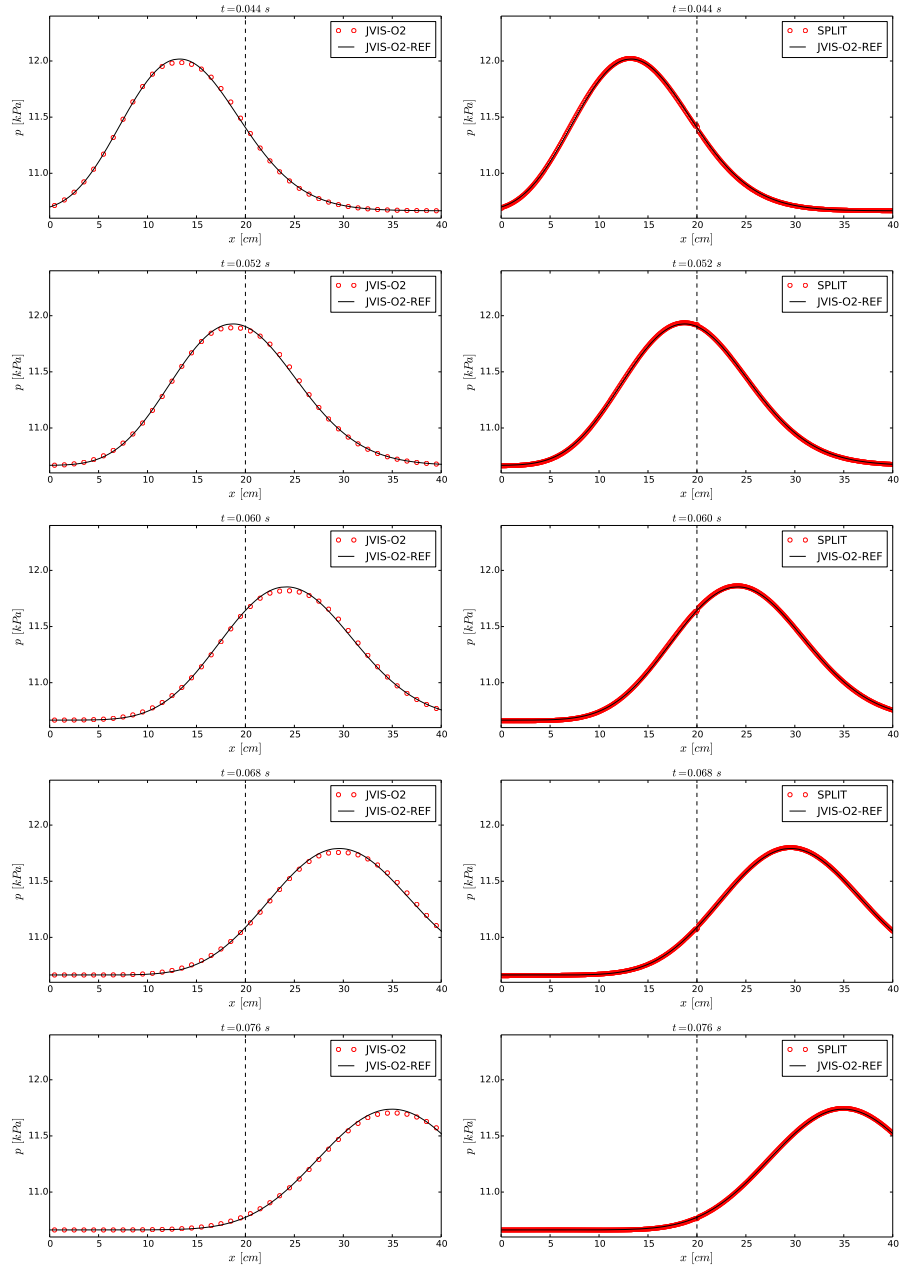

Figure 5: Test 2: pressure along vessels V2 and V3. *JVIS-O2*: solution obtained with a second order implementation of the proposed methodology; *SPLIT*: solution obtained with the operator splitting technique; *JVIS-O2-REF*: solution obtained using the proposed methodology and $\Delta x = 1\,mm$. Dashed line shows the location of the junction.

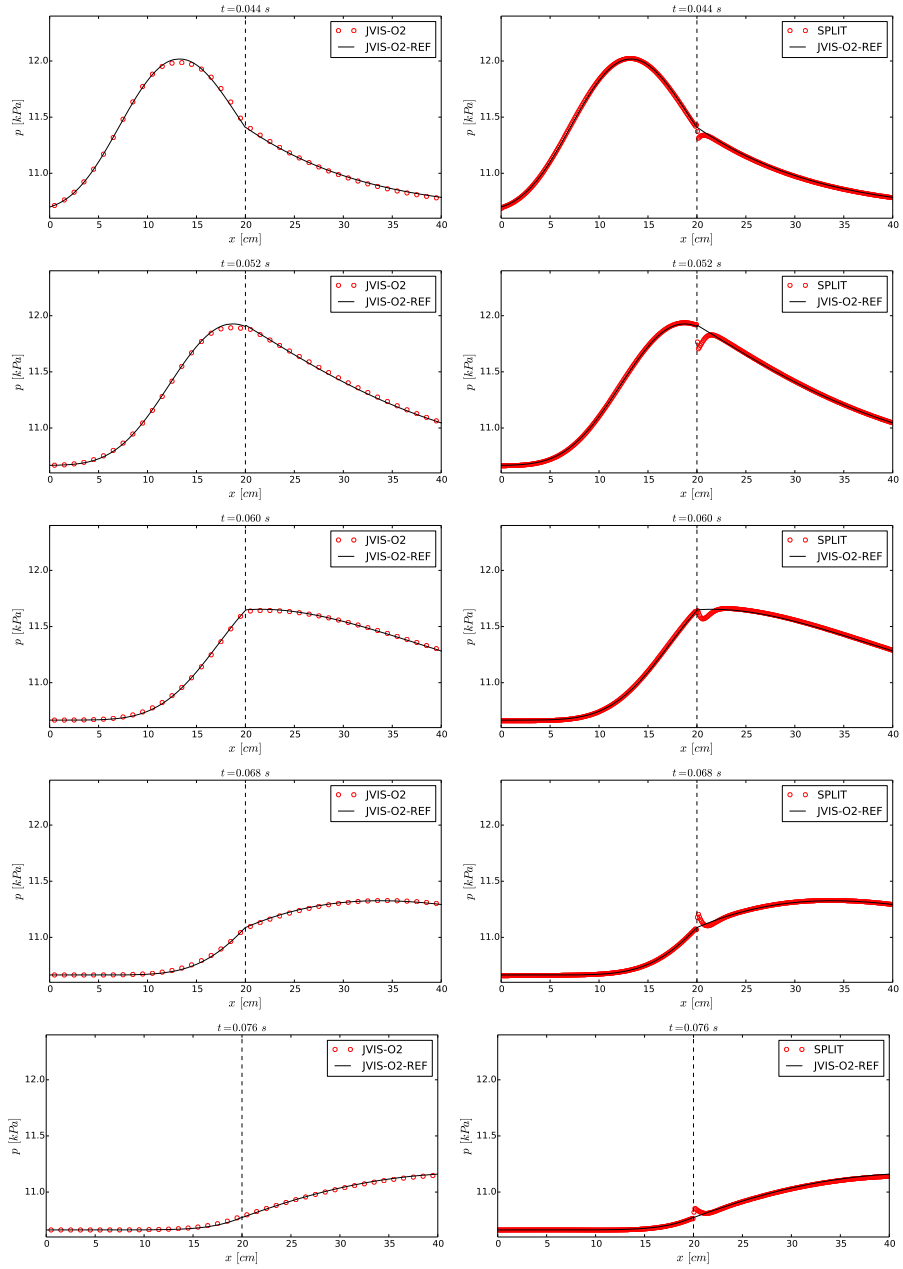

Figure 6: Test 2: pressure along vessels V2 and V4. *JVIS-O2*: solution obtained with a second order implementation of the proposed methodology; *SPLIT*: solution obtained with the operator splitting technique; *JVIS-O2-REF*: solution obtained using the proposed methodology and $\Delta x = 1\,mm$. Dashed line shows the location of the junction.

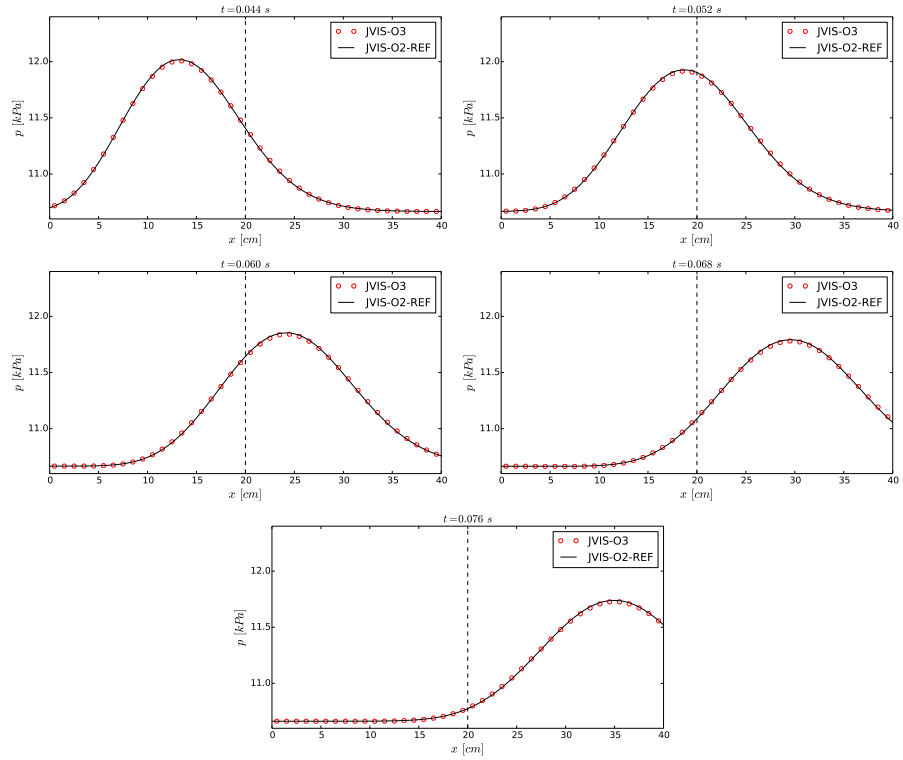

Figure 7: Test 2: pressure along vessels V2 and V3. *JVIS-O3*: solution obtained with a third order implementation of the proposed methodology; *JVIS-O2-REF*: solution obtained using the proposed methodology and $\Delta x = 1 mm$. Dashed line shows the location of the junction.

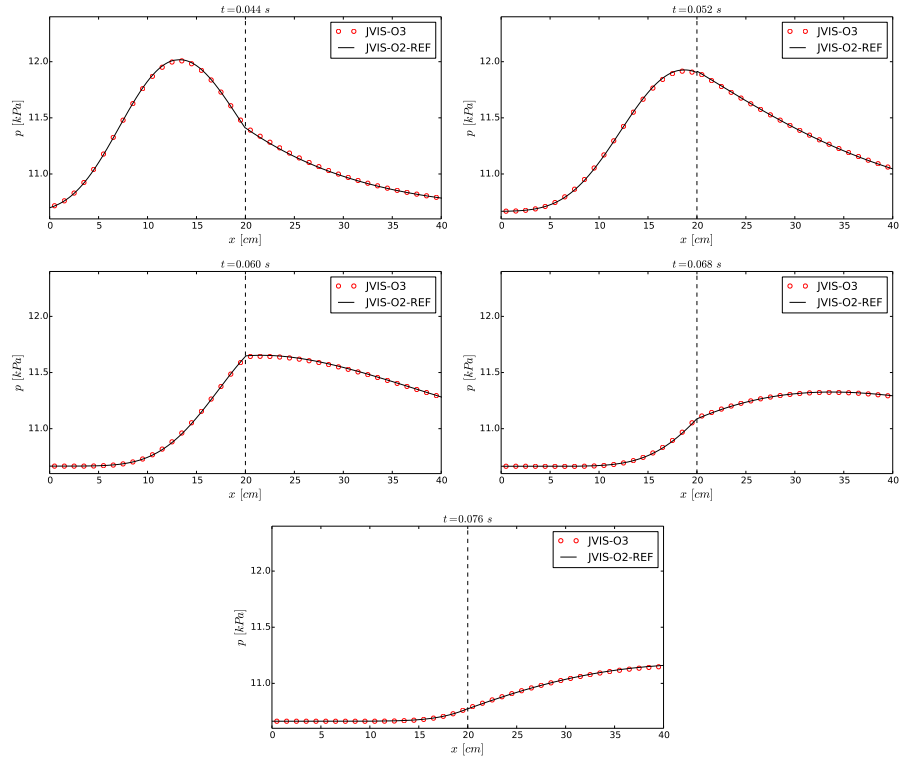

Figure 8: Test 2: pressure along vessels V2 and V4. *JVIS-O3*: solution obtained with a third order implementation of the proposed methodology; *JVIS-O2-REF*: solution obtained using the proposed methodology and $\Delta x = 1 mm$. Dashed line shows the location of the junction.

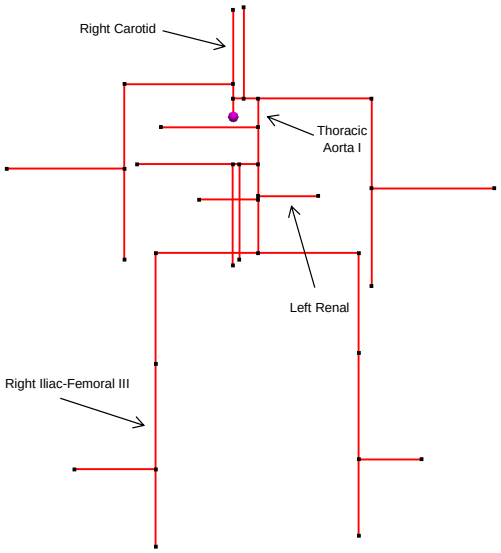

Figure 9: Schematic representation of the *in vitro* model of the arterial system presented in [33]. The purple circle indicates the root of the aorta, where an inflow boundary condition is prescribed. Terminal edges of vessels are linked to purely resistive elements. Vessels at which the solution is sampled are evidenced by black arrows.

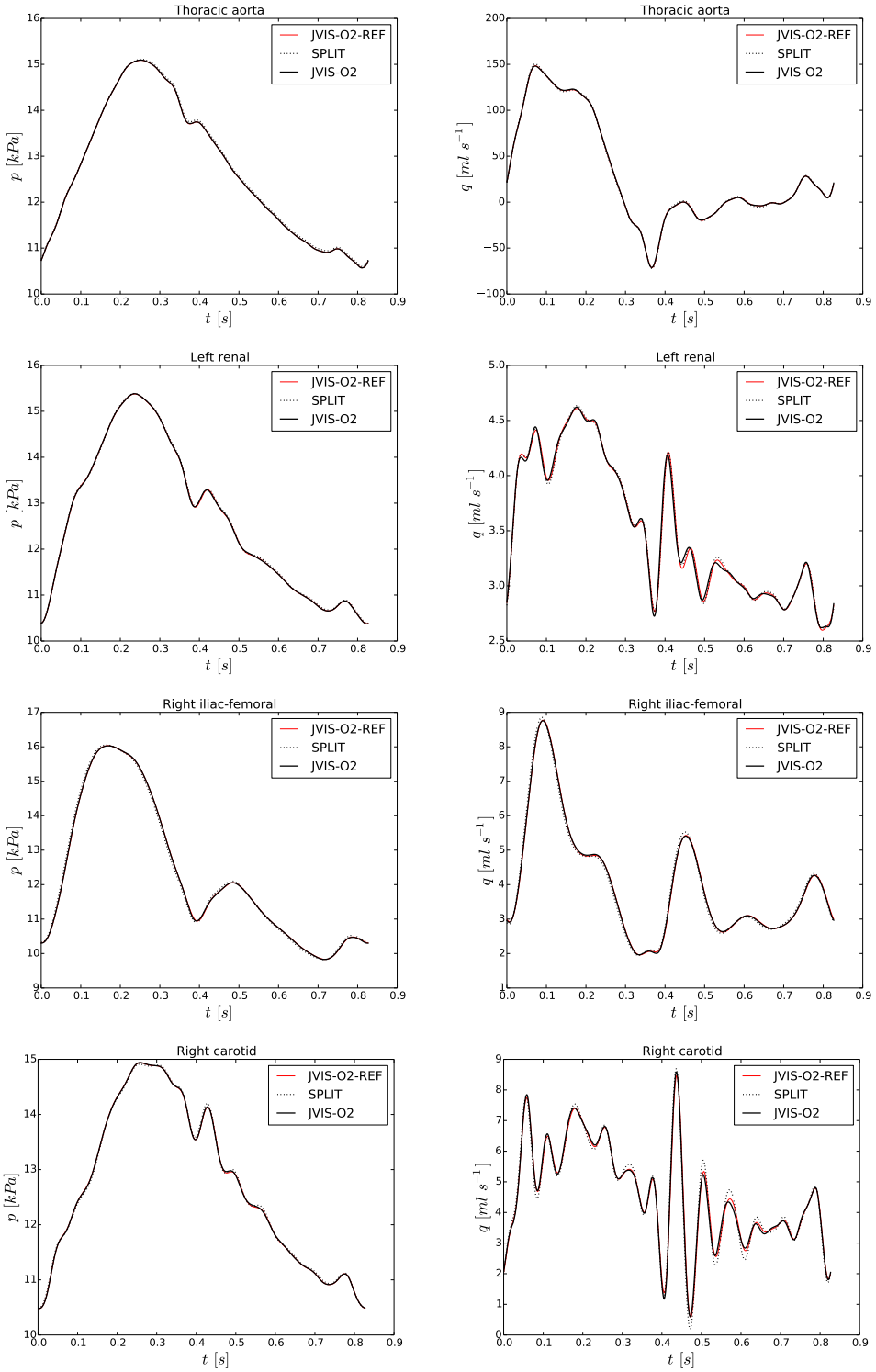

Figure 10: Pressure (left) and flow (right) for selected vessels of the *in vitro* arterial network model. *JVIS-O2*: solution obtained with a second order implementation of the proposed methodology; *SPLIT*: solution obtained with the operator splitting technique; *JVIS-O2-REF*: solution obtained using the proposed methodology and $\Delta x = 5\,mm$.

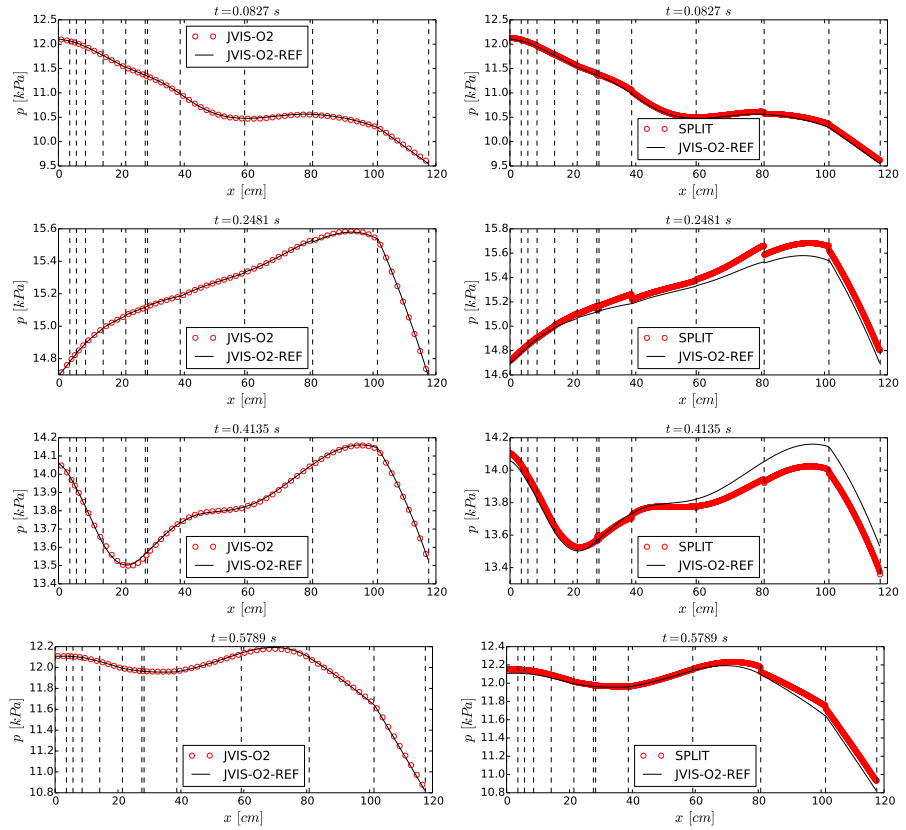

Figure 11: Pressure along the aorta and lower limb of the *in vitro* arterial network model at selected time instants. *JVIS-O2*: solution obtained with a second order implementation of the proposed methodology; *SPLIT*: solution obtained with the operator splitting technique; *JVIS-O2-REF*: solution obtained using the proposed methodology and $\Delta x = 5\,mm$. Dashed lines show the location of junctions.

Computational results shown in this section regard a spatial discretization of $\Delta x = 20\,mm$ for the proposed methodology and of $\Delta x = 1\,mm$ for the operator splitting technique. A reference solution was obtained by using a mesh with $\Delta x = 5\,mm$ and the proposed methodology. A second order implementation of the proposed methodology was used. As for the previous section, a minimal number of three and one computational cells per vessel was imposed for the operator splitting technique and for the proposed methodology, respectively. A $CFL = 0.9$ was used and the relaxation time T was allowed to be different for each vessel in order to ensure that $\triangle = 1$ over the entire network.

Figure 13 shows pressure and flow over the cardiac cycle at the midpoint of selected vessels. According to the diameter of each artery and to the parametrization criteria (68), the brachial and ulnar arteries have a very low viscoleasticity ($K_m = 30Pas$), whereas the posterior interosseous and the deep brachial arteries are highly viscoelastic ($K_m = 16500Pas$). In fact, the effect of viscoelasticity is more pronounced in the two latter vessels, where the attenuation of the flow waveform can be clearly observed for the case of the proposed methodology. Flow waveforms for the operator splitting technique tend to have a similar shape to the one obtained neglecting viscoelasticity everywhere in the network, denoted by *ELAS* in Figure 13. Moreover, the effect of viscoelasticity can be seen in pressure waveforms obtained for large (elastic) and small (viscoelastic) vessels. Small vessels will be stiffer during the loading phase, and they will in turn influence the flow in the larger artery. This is confirmed by results depicted in Figure 14. Here we show how cross-sectional area in viscoelastic vessels is lower if compared to the elastic case (even for larger pressure values), *i.e.* the vessel is stiffer in the loading phase, whereas in vessels with low viscoelasticity there is a higher distension, due to the influence of small arteries along its course.

As for the case of the *in vitro* network, it is useful to consider the spatial plot of pressure along the network at certain instants of the cardiac cycle, as shown in Figure 15. As in the previous case, it is evident that the proposed methodology achieves a nearly mesh-independent solution with a relative coarse mesh ($\Delta x = 20\,mm$), whereas the solution obtained by the operator splitting technique will suffer from physical inconsistency due to neglecting viscoleasticity at junctions. Of course border effects will be more evident in small vessels, as for the case presented in Section 4.2. However, perhaps the most relevant aspect here is that, for networks with highly viscoelastic vessels, an incorrect treatment of junctions can have an appreciable impact not only on small arteries, but also on waveforms of large arteries.

5. Final remarks

We have proposed a coupling strategy for one-dimensional blood flow in viscoelastic vessels based on a hyperbolic reformulation of the original convection-diffusion-reaction system and on the interpretation of junctions/bifurcations as Riemann problems for which an approximate/exact solver can be devised. The accuracy of the methodology was assessed by empirical convergence tests and by solving the simplest possible problem for which an equivalent solution exists, the passage of a pressure wave across a junction of two vessels with identical mechanical and geometrical properties. Moreover, we assessed the impact of neglecting viscoleasticity at junctions for simple and anatomically detailed arterial networks, showing that the proposed methodology preserves the consistency and accuracy of the numerical methodology used to solve the partial differential equations within the one-dimensional domain. Comparisons where made versus results obtained using the operator splitting technique. From the results presented in this work, it is evident that neglecting viscoelasticity at junctions can have a significant impact on the physical consistency and numerical accuracy of the solution delivered by the numerical scheme. In relation to this last point, we would like to notice that, to the best of our knowledge, a comprehensive study on the impact of viscoelasticity in one-dimensional blood flow models for small and large vessel networks

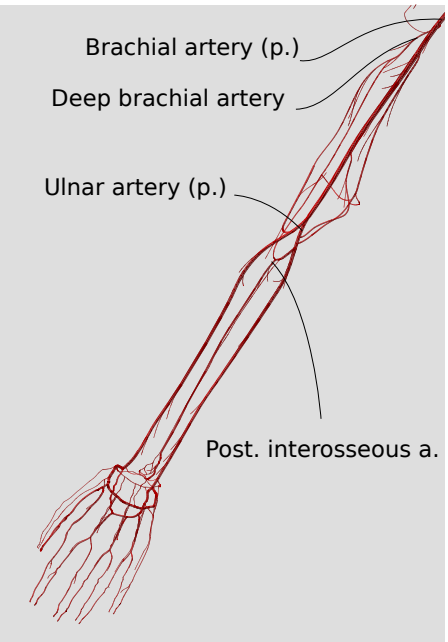

Figure 12: Anatomically detailed network of the upper limb presented in [34]. Names of arteries regard vessels for which time-pressure/flow plots are latter displayed.

would be of great interest for practitioners in this field. We believe that such study, on the light of the conclusions from this work, is even more mandatory in view of the strong impact that an inconsistent treatment of the viscoelasticity can have on the solution, with misleading conclusions about its true effect. This subject is the matter of current investigation and will be addressed in future communications.

Acknowledgements

The authors wish to thank Prof. Enrique Zuazua for useful discussions that contributed to the improvement of the manuscript.

This work was partially supported by the Brazilian agencies CNPq and FAPERJ. The support of these agencies is gratefully acknowledged.

6. References

References

[1] Y. Zocalo, D. Bia, S. Lluberas, R. L. Armentano, Regional differences in veins wall viscosity, compliance, energetics and damping: analysis of the pressure-diameter relationship during cyclical overloads, Biological Research 41 (2008) 227–233.

[2] R. L. Armentano, J. G. Barra, J. Levenson, A. Simon, R. H. Pichel, Arterial wall mechanics in conscious dogs: Assessment of viscous, inertial, and elastic moduli to characterize aortic wall behavior, Circulation Research 76 (3) (1995) 468–478.

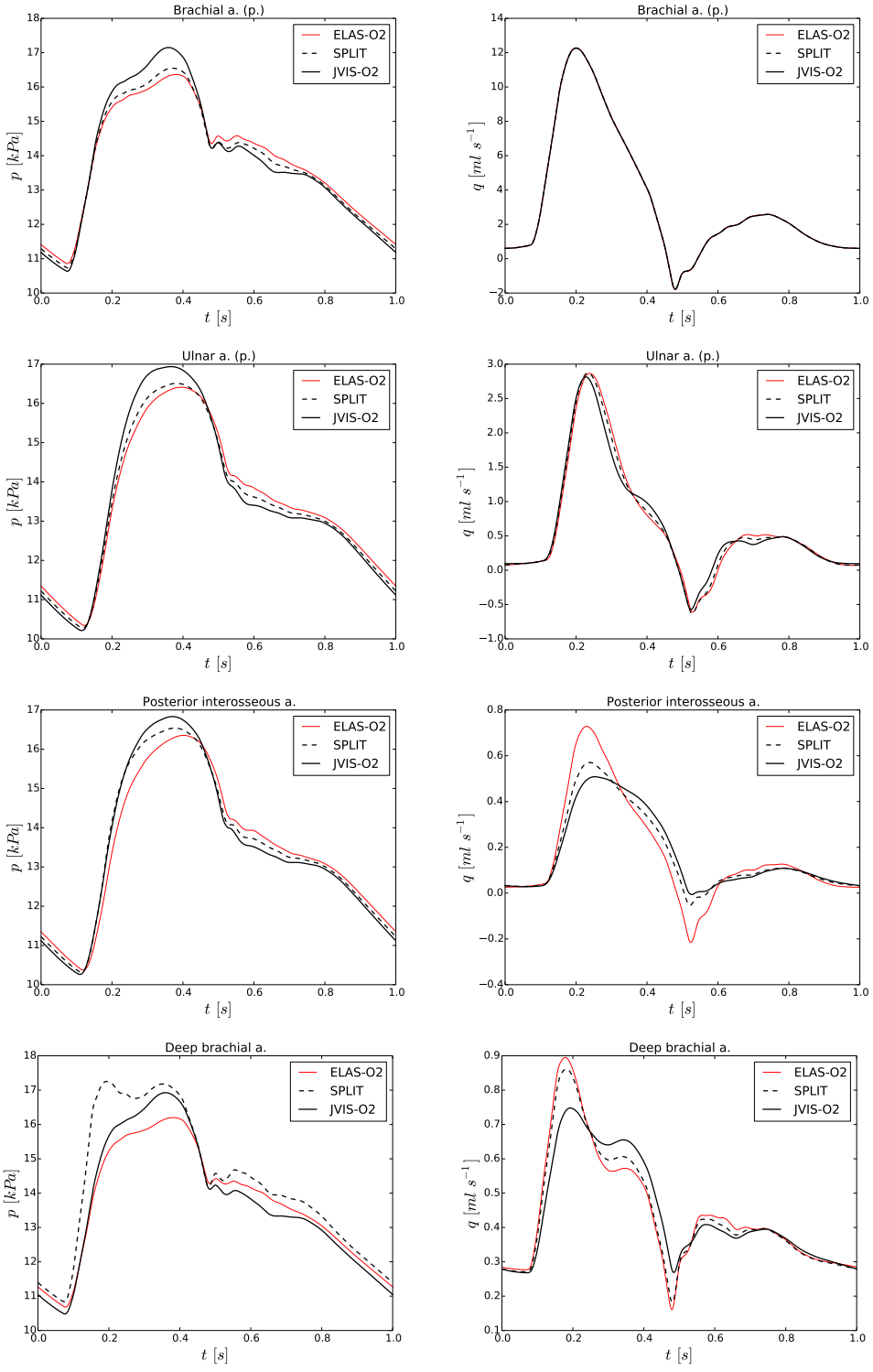

Figure 13: Pressure (left) and flow (right) for selected vessels of the ADAN arm network. *ELAS-O2*: solution obtained with a second order implementation of the proposed methodology and $K_m = 0$; *JVIS-O2*: solution obtained with the proposed methodology; *SPLIT*: solution obtained with the operator splitting technique.

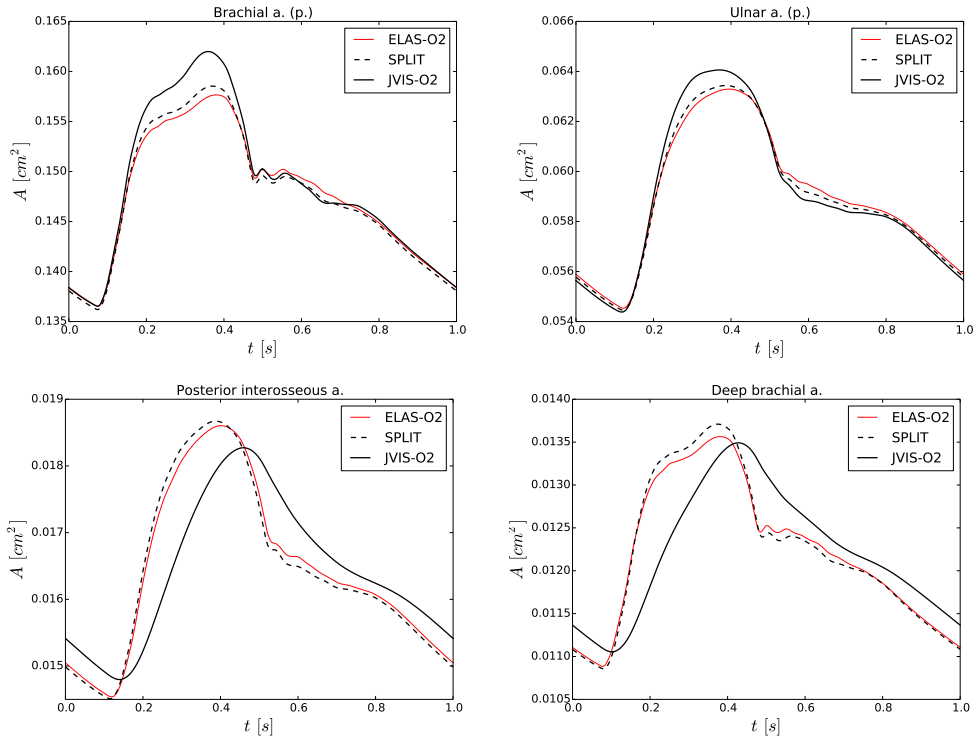

Figure 14: Cross-sectional area over the cardiac cycle for selected vessels of the ADAN arm network. *ELAS-O2*: solution obtained with a second order implementation of the proposed methodology and $K_m = 0$; *JVIS-O2*: solution obtained with the proposed methodology; *SPLIT*: solution obtained with the operator splitting technique.

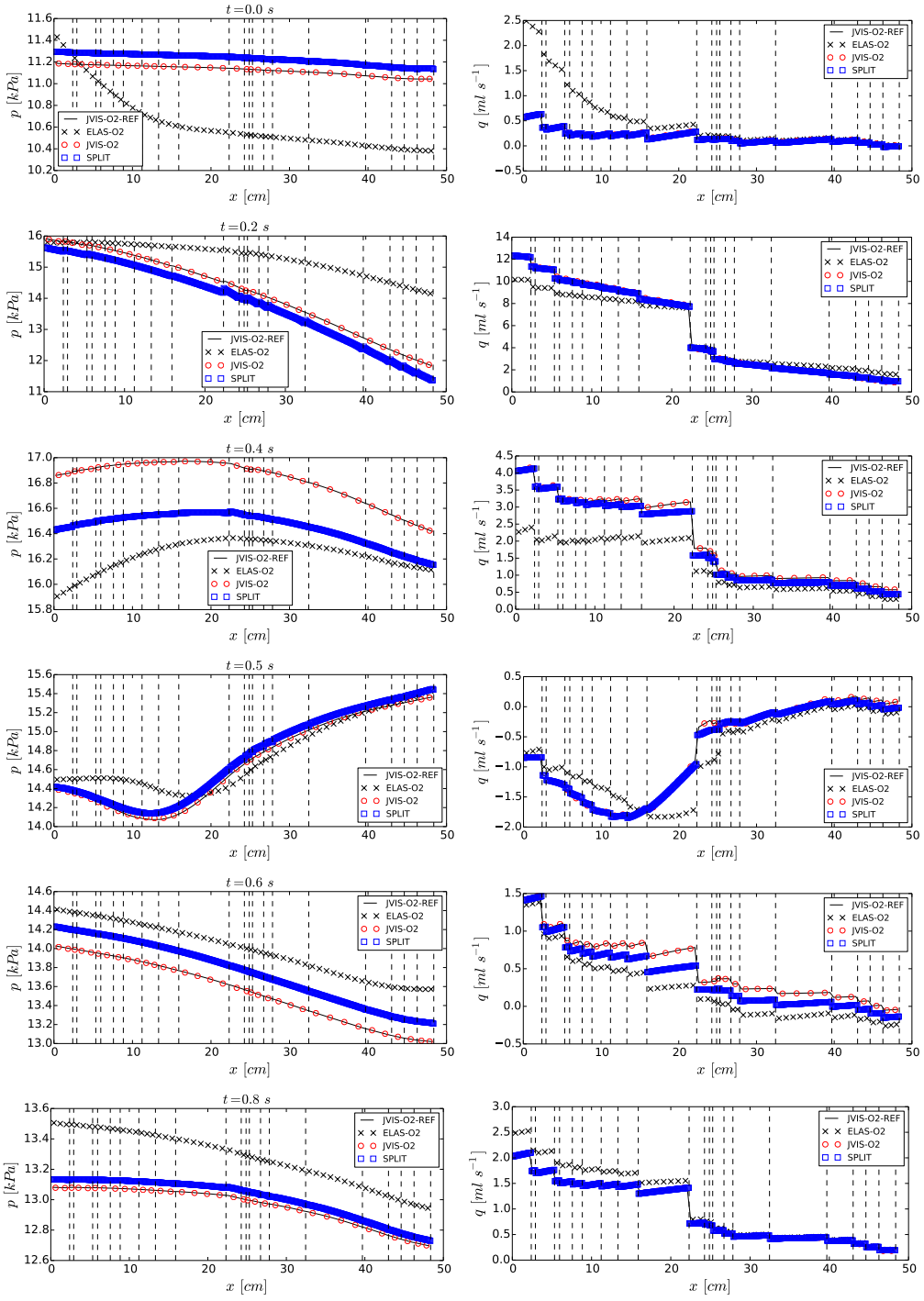

Figure 15: Pressure (left) and flow (right) along the brachial and ulnar arteries of the ADAN arm network. *ELAS-O2*: solution obtained with a second order implementation of the proposed methodology and $K_m = 0$; *JVIS-O2*: solution obtained with the proposed methodology; *SPLIT*: solution obtained with the operator splitting technique. *JVIS-O2-REF*: solution obtained using the proposed methodology and $\Delta x = 5\,mm$. Dashed lines show the location of junctions.

[3] D. Valdez-Jasso, M. A. Haider, H. T. Banks, D. B. Santana, Y. Zócalo, R. L. Armentano, M. S. Olufsen, Analysis of Viscoelastic Wall Properties in Ovine Arteries, IEEE Transactions on Biomedical Engineering 56 (2009) 210–219.

[4] N. Westerhof, A. Noordergraaf, Arterial viscoelasticity: A generalized model: Effect on input impedance and wave travel in the systematic tree, Journal of Biomechanics 3 (3) (1970) 357 – 379.

[5] D. Bia, R. L. Armentano, J. C. Grignola, D. Cralem, Y. A. Zócalo, F. F. Ginés, J. Levenson, The vascular smooth muscle of great arteries: Local control site of arterial buffering function, Revista Españla de Cardilogía 56 (2003) 1202–1209.

[6] B. C. L. Barnard, W. A. Hunt, W. P. Timlake, E. Varley, A theory of fluid flow in compliant tubes, Biophysical Journal 6 (1966) 717–724.

[7] T. J. Hughes, J. Lubliner, On the One-Dimensional Theory of Blood Flow in the Large Vessels Mathematical, Biosciences 18 (1973) 161–170.

[8] A. P. Avolio, Multi-branched model of the human arterial system, Medical and Biological Engineering and Computing 18 (1980) 709–718.

[9] N. Stergiopulos, D. F. Young, T. R. Rogge, Computer simulation of arterial flow with applications to arterial and aortic stenoses, Journal of Biomechanics 25 (12) (1992) 1477 – 1488.

[10] P. Reymond, F. Merenda, F. Perren, D. Rüfenacht, N. Stergiopulos, Validation of a one-dimensional model of the systemic arterial tree, American Journal of Physiology - Heart and Circulatory Physiology 297 (2009) H208–H222.

[11] F. Y. Liang, S. Takagi, R. Himeno, H. Liu, Biomechanical characterization of ventricular-arterial coupling during aging: A multi-scale model study, Journal of Biomechanics 42 (2009) 692–704.

[12] P. J. Blanco, S. M. Watanabe, E. A. Dari, M. R. F. Passos, R. A. Feijóo, Blood flow distribution in an anatomically detailed arterial network model: criteria and algorithms, Biomechanics and Modeling in Mechanobiology 13 (2014) 1303–1330.

[13] P. J. Blanco, S. M. Watanabe, M. R. F. Passos, P. A. Lemos, R. A. Feijóo, An anatomically detailed arterial network model for one-dimensional computational hemodynamics, IEEE Transactions on Biomedical Engineering 62 (2015) 736–753.

[14] L. O. Müller, E. F. Toro, A global multiscale mathematical model for the human circulation with emphasis on the venous system, International Journal for Numerical Methods in Biomedical Engineering 30 (2014) 681–725.

[15] L. O. Müller, E. F. Toro, An enhanced closed-loop model for the study of cerebral venous blood flow, Journal of Biomechanics 47 (2014) 3361–3372.

[16] J. Mynard, J. Smolich, One-dimensional haemodynamic modeling and wave dynamics in the entire adult circulation, Annals of Biomedical Engineering (2015) 1–18.

[17] J. Alastruey, K. H. Parker, J. Peiró, S. M. Byrd, S. J. Sherwin, Modelling the circle of Willis to assess the effects of anatomical variations and occlusions on cerebral flows, Journal of Biomechanics 40 (2007) 1794–1805.

[18] J. Alastruey, T. Passerini, L. Formaggia, J. Peiró, Physical determining factors of the arterial pulse waveform: theoretical analysis and calculation using 1-D formulation, Journal of Engineering Mathematics 77 (2012) 19–37.

[19] F. Y. Liang, K. Fukasaku, H. Liu, S. Takagi, A computational model study of the influence of the anatomy of the circle of willis on cerebral hyperperfusion following carotid artery surgery, BioMedical Engineering OnLine 10 (1) (2011) 84.

[20] J. Mynard, J. Smolich, The case against the reservoir-wave approach, International Journal of Cardiology 176 (2014) 1009–1012.

[21] P. J. Blanco, M. R. Pivello, S. A. Urquiza, R. A. Feijóo, On the potentialities of 3D-1D coupled models in hemodynamics simulations, Journal of Biomechanics 42 (2009) 919–930.

[22] P. J. Blanco, P. R. Trenhago, L. G. Fernandes, R. A. Feijóo, On the integration of the baroreflex control mechanism in a heterogeneous model of the cardiovascular system 28 (4) (2012) 412–433.

[23] L. Müller, E. Toro, E. Haacke, D. Utriainen, Impact of CCSVI on cerebral haemodynamics: a mathematical study using MRI angiographic and flow data, Phlebology, in press.

[24] E. F. Toro, L. O. Müller, M. Cristini, E. Menegatti, P. Zamboni, Impact of jugular vein valve function on cerebral venous haemodynamics, Current Neurovascular Research 12 (2015) 1–12.

[25] J. Alastruey, A. W. Khir, K. S. Matthys, P. Segers, S. J. Sherwin, Pulse wave propagation in a model human arterial network: Assessment of 1-D visco-elastic simulations against *in vitro* measurements, Journal of Biomechanics 44 (2011) 2250–2258.

[26] A. C. I. Malossi, P. Blanco, S. Deparis, A two-level time step technique for the partitioned solution of one-dimensional arterial networks, Computer Methods in Applied Mechanics and Engineering 237-240 (2012) 212–226.

[27] R. Raghu, I. E. Vignon-Clementel, C. A. Figueroa, C. A. Taylor, Comparative Study of Viscoelastic Arterial Wall Models in Nonlinear One-Dimensional Finite Element Simulations of Blood Flow, Journal of Biomechanical Engineering 133 (2011) 081003-1–081003-11.

[28] X. Wang, J.-M. Fullana, P.-Y. Lagrée, Verification and comparison of four numerical schemes for a 1d viscoelastic blood flow model, Computer Methods in Biomechanics and Biomedical Engineering 18 (15) (2015) 1704–1725.

[29] L. Itu, P. Sharma, A. Kamen, C. Suciu, D. Comaniciu, A novel coupling algorithm for computing blood flow in viscoelastic arterial models, in: Engineering in Medicine and Biology Society (EMBC), 2013 35th Annual International Conference of the IEEE, 2013, pp. 727–730.

[30] T. Passerini, M. de Luca, L. Formaggia, A. Quarteroni, A. Veneziani, A 3d/1d geometrical multiscale model of cerebral vasculature, Journal of Engineering Mathematics 64 (2009) 319–330.

[31] G. Montecinos, L. Müller, E. F. Toro, Hyperbolic reformulation of a 1D viscoelastic blood flow model and ADER finite volume schemes, Journal of Computational Physics 266 (2014) 101–123.

[32] L. O. Müller, P. J. Blanco, A high order approximation of hyperbolic conservation laws in networks: Application to one-dimensional blood flow, Journal of Computational Physics 300 (2015) 423 – 437.

[33] K. S. Matthys, J. Alastruey, J. Peiró, A. W. Khir, P. Segers, P. R. Verdonck, K. H. Parker, S. J. Sherwin, Pulse wave propagation in a model human arterial network: Assessment of 1-D numerical simulations against *in vitro* measurements, Journal of Biomechanics 40 (2007) 3476–3486.

[34] S. M. Watanabe, P. J. Blanco, R. A. Feijóo, Mathematical model of blood flow in an anatomically detailed arterial network of the arm, ESAIM: Mathematical Modelling and Numerical Analysis 47 (2013) 961–985.

[35] S. J. Sherwin, V. Franke, J. Peiró, K. H. Parker, One-dimensional modelling of a vascular network in space-time variables, Journal of Engineering Mathematics 47 (2003) 217–250.

[36] L. Formaggia, D. Lamponi, A. Quarteroni, One-dimensional models for blood flow in arteries, Journal of Engineering Mathematics 47 (2003) 251–276.

[37] R. Borsche, J. Kall, ADER schemes and high order coupling on networks of hyperbolic conservation laws, Journal of Computational Physics 273 (2014) 658 – 670.

[38] E. F. Toro, A. Siviglia, Flow in collapsible tubes with discontinuous mechanical properties: mathematical model and exact solutions, Communications in Computational Physics 13 (2) (2013) 361–385.

[39] R. J. LeVeque, Finite volume methods for hyperbolic problems, Cambridge texts in applied mathematics, Cambridge University Press, Cambridge, New York, 2002.

[40] L. O. Müller, E. F. Toro, Well-balanced high-order solver for blood flow in networks of vessels with variable properties, International Journal for Numerical Methods in Biomedical Engineering 29 (2013) 1388–1411.

[41] M. Dumbser, E. F. Toro, A Simple Extension of the Osher Riemann Solver to Non-conservative Hyperbolic Systems, Journal of Scientific Computing 48 (2011) 70–88.

[42] M. Dumbser, C. Enaux, E. F. Toro, Finite volume schemes of very high order of accuracy for stiff hyperbolic balance laws, Journal of Computational Physics 227 (2008) 3971–4001.

[43] M. Dumbser, M. Castro, C. Parés, E. F. Toro, ADER schemes on unstructured meshes for nonconservative hyperbolic systems: Applications to geophysical flows, Computers & Fliuds 38 (2009) 1731–1748.

[44] M. Dumbser, A. Hidalgo, M. Castro, C. Parés, E. F. Toro, FORCE schemes on unstructured meshes II: Non-conservative hyperbolic systems, Computer Methods in Applied Mechanics and Engineering 199 (2010) 625–647.

[45] M. Dumbser, M. Käser, Arbitrary high order non-oscillatory finite volume schemes on unstructured meshes for linear hyperbolic systems, Journal of Computational Physics 221 (2007) 693–723.

[46] A. Hidalgo, M. Dumbser, ADER Schemes for Nonlinear Systems of Stiff Advection-Diffusion-Reaction Equations, Journal of Scientific Computing 48 (2011) 173–189.

[47] E. F. Toro, Riemann Solvers and Numerical Methods for Fluid Dynamics: A Practical Introduction, 3rd Edition, Springer-Verlag, Berlin Heidelberg, 2009, ISBN 978-3-540-25202-3.

[48] E. F. Toro, V. A. Titarev, Derivative Riemann solvers for systems of conservation laws and ADER methods, Journal of Computational Physics 212 (2006) 150–165.

[49] E. F. Toro, V. A. Titarev, Solution of the generalized Riemann problem for advection-reaction equations, Proceedings of the Royal Society A 458 (2002) 271–281.